Engineering Structures 148 (2017) 63–80

Contents lists available at ScienceDirect

Engineering Structures

journal homepage: www.elsevier.com/locate/engstruct

Modeling cyclic inelastic in-plane flexural behavior of concrete filled sandwich steel panel walls

Erkan Polat [a,*], Michel Bruneau [b]

[a] Dept. of Civil, Structural and Environmental Engrg., Univ. at Buffalo, State Univ. of New York, 206 Ketter Hall, Buffalo, NY 14260, United States
[b] Dept. of Civil, Structural and Environmental Engrg., Univ. at Buffalo, State Univ. of New York, 130 Ketter Hall, Buffalo, NY 14260, United States

ARTICLE INFO

Article history:
Received 14 July 2016
Revised 2 June 2017
Accepted 9 June 2017

Keywords:
Steel-concrete composite walls
Sandwich walls
Seismic
Cyclic behavior
Finite element
Modeling
Composite behavior

ABSTRACT

Finite element analysis was first used to replicate the inelastic cyclic test response of previously tested concrete filled steel sandwich panel (CFSSP) walls, to determine the material and contact models best able to capture the wall's initial stiffness, the ultimate wall strength at each cycle, the web plate and HSS local buckling, and the pinching in the hysteresis loops. Results obtained show good agreement with all those aspects of response, while providing insights, guidance, and a validated model that will be of benefit in future studies of CFSSP-Walls. In a second part of this paper, the calibrated finite element model is used to provide insights and generate knowledge on some important aspects of wall behavior that is valuable for the design of CFSSP-Walls. Designers of CFSSP-Walls are typically provided little prescriptive guidance by design specifications and must instead rely, to a large extent, on findings from the recent research literature to ascertain that designs will perform as intended. For this new structural system, such insights into structural behavior are severely lacking. The findings here provide such insights on the distribution of wall-to-footing forces, shear force demands in critical tie bars, cumulative plastic strain value at failure due to low-cycle fatigue, the effect of hoop and shear stresses on uniaxial steel plate yielding, and the effect of interface friction on the force flow within boundary elements. These allow research to verify the adequacy of many of the assumptions used to determine the wall's plastic moment, which is typically considered to be the flexural strength of CFSSP-Walls.

1. Introduction

Concrete filled sandwich steel panel walls (CFSSP-Walls) are composed of two steel skin plates interconnected by tie bars, with the space between the skin plates filled with concrete. These walls are attractive for use in seismic regions, including as ductile flexural walls in high-rise applications, as they can be highly ductile, redundant, of high strength, and rapid to construct and thinner than corresponding conventional reinforced concrete (with resulting greater leasable space). Experimental and computational studies on CFSSP-Walls conducted by Alzeni and Bruneau [1,2] demonstrated that the strength of these walls can be conservatively predicted by the proposed plastic moment capacity that assumes uniform plastic stress distribution on the steel skin based on the yield strength of the steel, F_y, and the uniform compression strength of the concrete, f'_c. In that study, the general purpose finite element program ABAQUS [3] was used with the explicit objective of replicating initial wall stiffness and ultimate wall strength. Although the finite element model was able to match some of the specimens' experimentally measured flexural strength, it could not perfectly replicate the general shape of the hysteresis loops, such as the wall pinching and the peak strength at each cycle of loading. Furthermore, the modeling of strength degradation was achieved using a Concrete Damage Plasticity (CDP) material model with decreasing concrete compressive strength at larger strains with limited accuracy. However, by tracking behavior throughout the response, it was demonstrated in the finite-element simulations of thin-walled concrete-filled circular steel columns [4], and of concrete-filled double-skin tubes [5] that the opening and closing of concrete cracking is responsible for the pinching effect observed in the cyclic testing of such concrete-filled structural elements. This indicated a need to attempt replicating the experimental results of the CFSSP-Walls using more robust and physically accurate models and constitutive relationships, such as the Winfrith concrete model (currently available in LS-DYNA [6,7], but not in ABAQUS [8]) successfully used by Imani and Bruneau [5].

This paper first investigates how to best model CFSSP-Walls to replicate the inelastic cyclic experimental results obtained by

* Corresponding author.
E-mail addresses: erkanpol@buffalo.edu (E. Polat), bruneau@buffalo.edu (M. Bruneau).

http://dx.doi.org/10.1016/j.engstruct.2017.06.025
0141-0296/

Alzeni and Bruneau [1,2] using LS-DYNA. The goals of this part of the study are:

- To develop a robust finite element model that can be a reference in future analyses of CFSSP-Walls of any geometry, and;
- To investigate the effectiveness of the smear-crack Winfrith concrete model in capturing the pinching behavior of CFSSP-Walls;

The development of such a finite element model validated against the results of cyclic loading experiments was not as straight-forward as one might intuitively believe at first, and some aspects of modeling investigated in this paper are addressed to provide insights and guidance in this perspective. The availability of such a model will be of benefit in future studies of CFSSP-Walls. This will be particularly important to ensure reliable findings when investigating the behavior for other wall geometries, reducing the need for costly full-scale testing.

Furthermore, beyond the above, a significant part of this paper uses the developed model to generate knowledge on some important aspects of wall behavior that is informative and valuable for the design aspect of CFSSP-Walls. Note that designers of CFSSP-Walls are typically provided little prescriptive guidance by design specifications (such as, for example, Chapter H of AISC-341) and must instead rely, to a large extent, on findings from the recent research literature to ascertain that designs will perform as intended. For this new structural system, such insights into structural behavior are severely lacking. In that perspective, this study provides valuable insights into some aspects of behavior by:

- Investigating the distribution of wall base forces at the wall-footing connection for a specific type of footing to benefit future wall base connection design;
- Investigating the distribution of shear forces in tie bars following buckling of the CFSSP-Wall steel plate, because large shear forces could be detrimental to seismic performance of the structural system (and are currently not addressed by design provisions);
- Investigating and quantifying the effect of hoop and shear stresses on the uniaxial steel plate yield strength (per Von-Mises yield criterion) under cyclic wall displacement and increasing drift levels, to determine if these concurrent stresses could undermine the ability to attain the plastic moment (flexural strength) that engineers rely upon in their design;
- Determining the cumulative plastic strain value at failure due to low-cycle fatigue, which is missing knowledge essential to be able to analytically predict the ultimate failure of ductile CFSSP-Walls subjected to seismic response (which would typically be used in non-linear inelastic time-history analyses at the MCE level for these walls);
- Verifying the adequacy of the assumptions used to obtain the plastic moment (by examining the plastic neutral axis location and plane-stress distribution of the wall cross-section), to enhance confidence in using the plastic moment as the flexural design strength for those walls and visualizing how significant deviations are from the idealized model, and;
- Investigating and quantifying the effect of interface friction on the force flow within boundary elements to help engineers identify possible future situations where boundary elements' behavior might not be achievable without design alteration.

The above new knowledge, made possible by analyses using the validated finite element modeling approaches described here, provide structural design insights on some key aspects of CFSSP-Walls behavior.

2. CFSSP wall descriptions

Four CFSSP-Walls tested by Alzeni and Bruneau [1,2] were simulated using the general-purpose finite element software LS-DYNA [6] to further investigate static and cyclic in-plane behavior of CFSSP-Walls. Two of the tested specimens had boundary elements, referred to as Group B, and the other two had no boundary elements, referred to as Group NB. The respective cross-sections are illustrated in Fig. 1. The ends of Group B walls consisted of round HSS columns and their webs of double web skin plates having a width, w, of 30 in (762 mm)., a thickness, t, of 5/16 in (7.94 mm)., connected through circular tie bars spaced equally in both horizontal and vertical directions at a spacing, S, which varied from Specimen B1 to B2 as illustrated in Fig. 1(a). The ends of Group NB walls consisted of half round HSS columns and webs of double web skin plates having a width, w, of 40 in (1016 mm)., a thickness, t, of 5/16 in (7.94 mm), connected through circular tie bars spaced equally in both horizontal and vertical directions at a spacing, S, which varied from Specimen NB1 to NB2 as illustrated in Fig. 1 (b). The total cross-section depth of the B and NB specimens, W, were 44 in (1117.6 mm) and 48.625 in (1234.76 mm), respectively, and the height of the specimens above from their footing was 120 in (3048 mm). Note that the terminology "walls with boundary elements" and "without boundary elements" is kept here to ensure consistency with the information contained in the research report by Alzeni and Bruneau [1,2]. However, note that it is anticipated that in the AISC 341-16 seismic provisions (not yet published at the time of this writing), the term "boundary elements" will be used in a manner that encompasses both types of walls referred to here, and the term walls "without boundary elements" will refer to those that do not have any capping members or plates at their ends.

Illustrated in Fig. 1 is also the plastic stress distribution at the cross-section which is used here for calculation of the plastic moment, M_p, of the CFSSP-Walls based on the assumption that the stress distributions on the steel and concrete part of the cross-section are uniform, and taken as F_y and f'_c respectively for steel and concrete, where F_y is the yield strength of the steel skin, and f'_c is the compressive strength of the concrete. Alzeni and Bruneau [1,2] provided closed form equations for the plastic moments; these are presented in Table 1. In Table 1 and Fig. 1, C is the depth of the compression zone on web plate (see Fig. 2), which is calculated from the vertical force equilibrium in the cross-section; b is the depth of the steel plate, t_c is the thickness of the concrete in the web of the wall, d_{in} is the inner diameter of the HSS section and other parameters are as defined previously.

The tested specimens were cantilever-type walls embedded into a reinforced concrete footing, itself connected to the strong floor using post-tensioned DYWIDAG bars. Fig. 2 illustrates the elevation and plan view of one of the CFSSP-Wall specimen. The thickness of the foundation was 24 in (609.6 mm) to accommodate the length of the available DYWIDAG bars. The foundation and DYWIDAG bars assembly were designed to sustain an overstrength moment equal to $1.5Mp = 3402$ kip-ft (4612.5 kN-m) moment and a corresponding shearing force of 340 kips (1512.4 kN). The DYWIDAG bars had a diameter of 1–3/8 in (34.93 mm) and were pre-tensioned to a force of 119 kips (529.3 kN) (corresponding to 63% of their yield load). The expected shearing force and the corresponding moment of the tested specimens were transferred to the footing using re-bars (denoted as connector re-bars) and annular rings. The connector re-bars were assumed to act as shear connectors, passing through the part of the wall embedded in the footing, normal to the steel web. The round HSS and double web plates were expected to develop their yield strength, and the forces generated due to yielding of the HSS part of the cross-section were

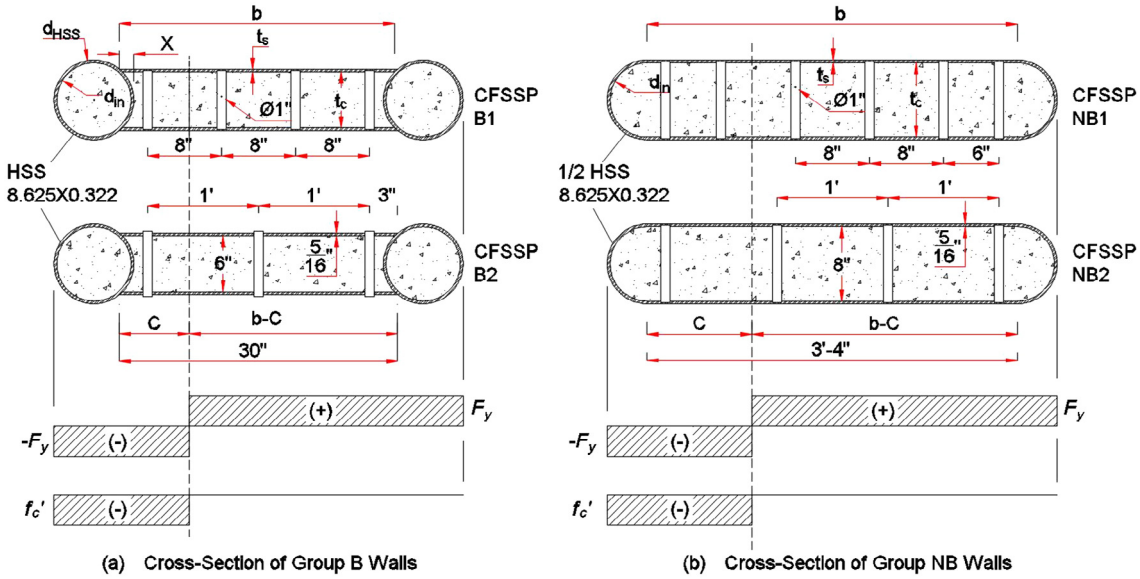

Fig. 1. Cross-sectional dimensions of CFSSP-Walls and stress blocks used to calculate flexural strengths of CFSSP-Walls: (a) Group B walls; (b) Group NB walls.

Table 1
Plastic moment capacity of concrete filled steel sandwich panels.

CFSSP	*Depth of compression zone (C) and plastic moment capacity (M_p)
NB	$M_p = 0.5A_{HSS}F_{yHSS}\left(\frac{2d_{HSS}}{\pi}+b\right)+[b^2+2C^2-2Cb]t_sF_{yweb}+\left(\frac{2d_{in}^2+3\pi d_{in}^2C}{24}+\frac{C^2t_c}{2}\right)f_c$
	$C=\frac{2bt_sF_{yweb}-0.125(\pi d_{in}^2)f_c}{4t_sF_{yweb}+t_cf_c}$
B	$M_p = A_{HSS}F_{yHSS}(b-2X+d_{HSS})+[b^2+2C^2-2Cb]t_sF_{yweb}+[0.25\pi d_{in}^2(0.5d_{HSS}+C-X)+0.33Xt_c(C-0.67X)+0.5t_c(C-X)^2]f_c$
	$X=0.5\left(d_{in}-\sqrt{d_{in}^2-t_c^2}\right)$
	$C=\frac{2bt_sF_{yweb}+(0.67Xt_c-0.25\pi d_{in}^2)f_c}{4t_sF_{yweb}+t_cf_c}$

* C is the depth of the compression zone on the web plate.

transferred through the annular ring (welded at the base of the round HSS) such as to transfer the tension forces at the toe of the CFSSP-Walls to the footing. The thickness of the annular ring was 1 in (25.4 mm) and stiffeners were used to minimize annular ring thickness.

3. Finite element modeling

Finite element simulations of the tested specimens were performed by Alzeni and Bruneau [1,2] using the computer program ABAQUS [3], with the explicit objectives of only replicating initial stiffness and maximum strength. Those analyses considering values of the elastic modulus of the concrete ranging from 0.5 to 0.8 of the E_c value given by the ACI [9] equation for regular concrete ($E_c = 57000\sqrt{f'_c}psi$) showed that the best match with the experimental stiffness results were obtained for 0.8 E_c. The finite element models were able to approximately capture the ultimate capacity of some of the specimens (some specimens' capacity were underestimated) and reasonably replicate the elastic stiffness and ductility of the CFSSP-Walls. Fig. 3 shows a typical comparison of experimentally obtained force-displacement hysteretic relationships with the one obtained from the ABAQUS model. The experimentally observed pinching in the force-displacement hysteretic curves were not captured by the ABAQUS model. As mentioned earlier, in those models, the strength degradation was achieved by using a CDP material model that exhibited degrading strength, even though strength degradation in the specimen actually occurred due to fracture of the steel shells (it was also reported that the numerical model exhibited strength degradation faster than observed in the tested specimen after local buckling of the steel web plate occurred). Furthermore, the CDP model does not consider smeared cracking (used in conventional concrete models [4,10]) under tensile stresses; rather, an isotropic plasticity model is assumed in both tension and compression [4]. However, past research on concrete-filled steel columns has shown that it is the opening and subsequent closing behavior of horizontal concrete cracks transverse to the column axis that create the pinching behavior in these columns (with stiffness being recovered as the cracks close), as explained by Goto et al. [4] and Imani and Bruneau [5]. While Goto et al. [4] used a modified concrete model by inserting a horizontal discrete crack model, Imani and Bruneau [5] showed that better agreement with experimental results could be obtained by using the Winfrith concrete model (available in LS-DYNA, not in ABAQUS at the time of this writing). The Winfrith concrete model considers smeared cracking, and has a crack width formulation [11] that accounts for various concrete parameters (i.e., aggregate size, concrete compressive strengths, loading rates, cement-to-water ratios, and test specimen size), as explained by Schwer [12]. The Winfrith concrete model has also been used since to simulate in-plane behavior of steel-plate concrete (SC) composite shear walls (without boundary elements) with aspect ratios of 0.6 to1.0 [13,14]. However, at the time of writing, the Winfrith concrete model has not been used to model flexural CFSSP-Walls of the type considered here, able to reach their full plastic moment (i.e., having an aspect-ratio greater than 2), with or without boundary elements.

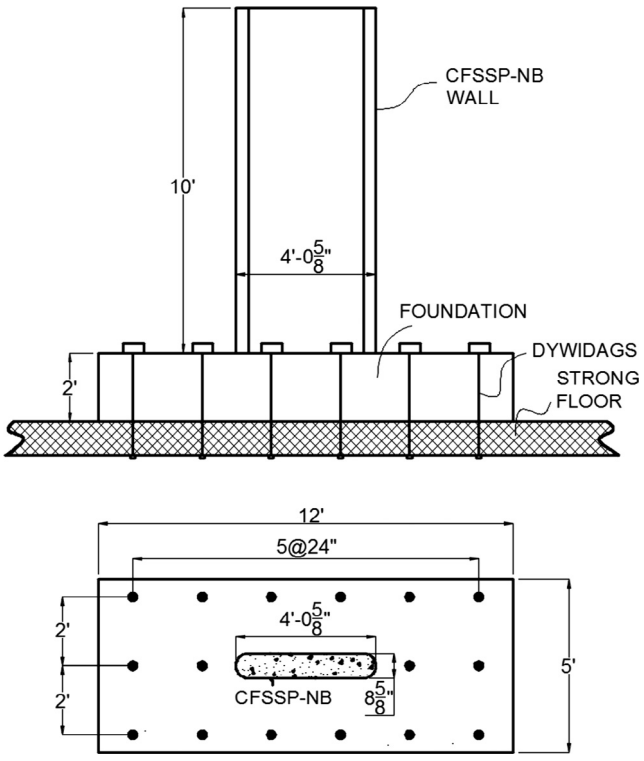

Fig. 2. Elevation and plan view of the CFSSP-NB wall model.

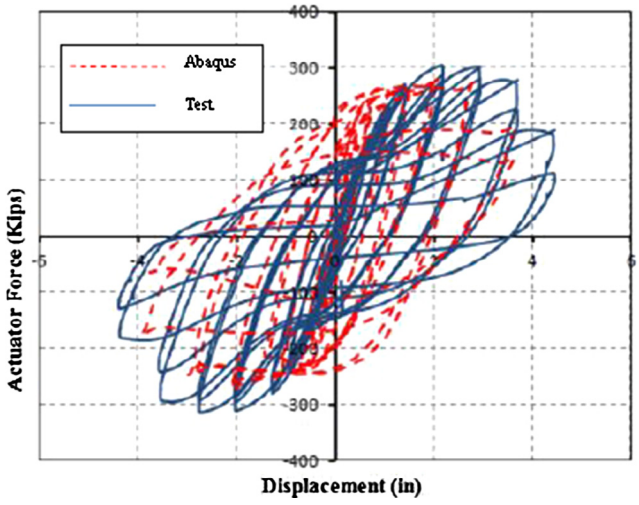

Fig. 3. Force displacement relationship for specimen CFSSP-NB1, ABAQUS versus test values (Alzeni and Bruneau [1]).

3.1. LS-DYNA models

LS-DYNA finite element models were developed for the four CFSSP-Wall specimens described above. Fig. 4 shows a representative LS-DYNA model for the CFSSP-B1 specimen illustrating the solid, shell, and beam elements used in parts of the model. The concrete infill was modeled using an eight-node constant stress solid element (*Solid 1*) with reduced integration, and *Winfrith_concrete* model (*Mat 084/085*). The size of the solid elements was $1 \times 1 \times 1$ in ($25.4 \times 25.4 \times 25.4$ mm). The steel sandwich panels and HSS were modeled using a four node fully integrated shell element (*Shell 16*) with Belytschko-Tsay shell formulation with three integration points through thickness, and the *plastic_kinematic*

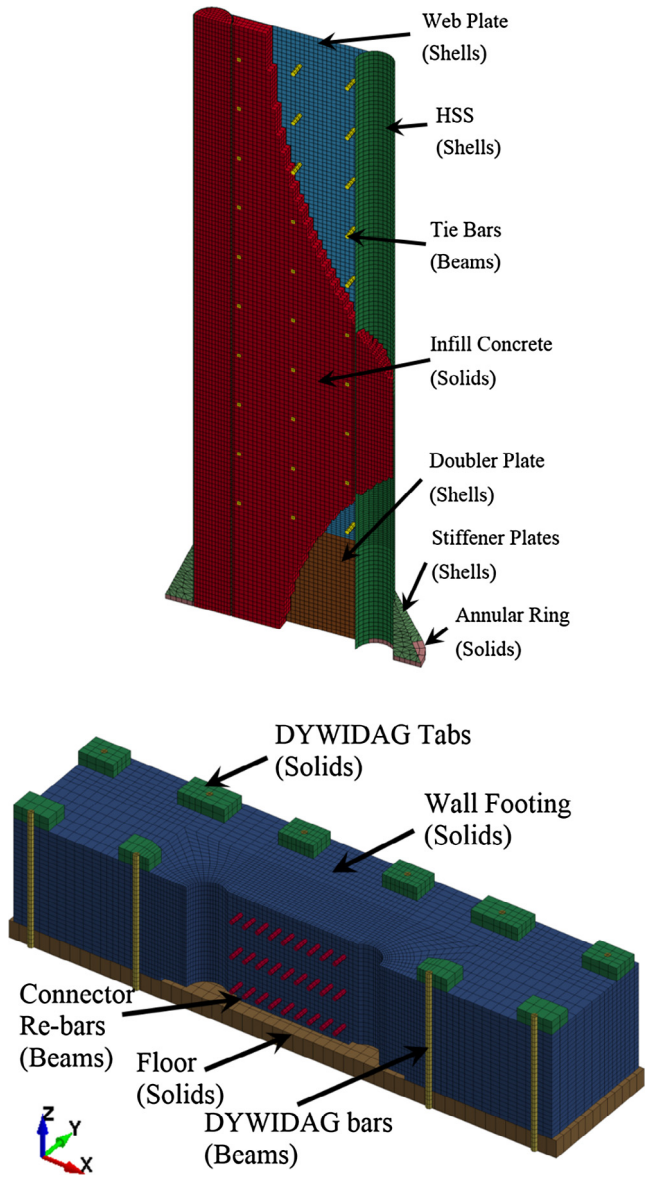

Fig. 4. LS-DYNA model.

(*Mat 003*) bilinear material model with kinematic hardening. The shell elements were 1×1 in (25.4×25.4 mm), and had the thickness of steel panels. The kinematic and isotropic hardening of *Mat 003* with its input parameters is illustrated in Fig. 5. Material constants necessary to specify the *plastic_kinematic* model are the Elastic Modulus (E), Poisson's ratio, Tangent Modulus (E_T), and Hardening parameter (β). Note that for this material model, the failure strain for eroding elements can also be specified by defining an effective plastic strain at failure. If a failure strain is specified, the *Mat 003* element is eroded only after all the integration points reach the failure strain. Fig. 6 shows the typical idealized (bilinear) material models used for: (a) the steel web plate, and; (b) the HSS (superposed onto the stress-strain curves for the standard uniaxial tension tests coupons tested by Alzeni and Bruneau [1,2] for the steel panels and HSS). Table 2 provides the average values of material tests for the steel and concrete used in the specimens. Note that stress-strain data for the HSS (Fig. 6(b)) did not exhibit a yield plateau, which resulted in a 20% higher yield strength definition in the bilinear material model formulated to capture the strain hardening part of the stress-strain curve. The elastic modulus used in

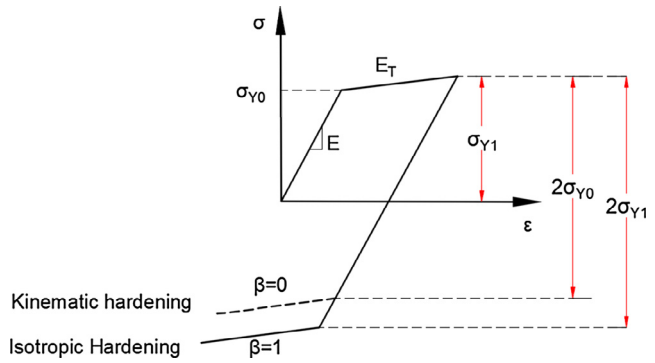

Fig. 5. *Mat_003* elastic-plastic material model with material hardening in LS-DYNA.

the simulations was 29,800 ksi (205,463 MPa) for the steel web and 27,500 ksi (189,605 MPa) for the HSS. For the web plate (WP) and HSS, as far as the other bilinear steel model parameters were concerned, Fy_{WP} of 62 (427), 64 (441), 61 (420), and 63 ksi (434 MPa), E_{T_WP} of 100 (689), 100 (689), 80 (551), and 110 ksi (758 MPa), Fy_{HSS} of 56 (386), 56 (386), 52 (358), and 51 ksi (351 MPa), and E_{T_HSS} of 80 (551), 60 (413), 50 (344) and 50 ksi (344 MPa) were used, for the models B1, B2, NB1, and NB2, respectively, where *Fy* is the yield strength and E_T the tangent modulus after yielding.

Given that the scope of work here is not on accurately modeling strength degradation, using a steel material model without damage parameters was deemed adequate for this particular study. The effect of fracture on strength degradation of the wall response under large deformations will be demonstrated by simulating HSS fracture by element erosion, an approach available for the steel material model used as described above. The cumulative plastic strain values at failure obtained from the finite element analyses at the drifts when cracking was first experimentally observed. However, note that cracks in the specimens were also first observed to initiate along (and propagate from) the plug weld of the tie bars [1,2], an entirely different and complex mechanism not modeled here.

The tie and reinforcing bars were modeled using two node beam elements (*Beam 1*) with the Hughes-Liu beam formulation with two integration points, and the *plastic_kinematic* material model. The beam elements had the diameter of the particular bar and were coupled with the shell elements of the steel sandwich panels by merging beam and shell mutual nodes, and similarly with the solid elements of the concrete infill by matching the length of the beam elements with the solid elements and merging the beam and solid mutual nodes. The tie bars used in the experiment have no reported measured stress-strain relationship, therefore an arbitrary bilinear curve with 50 ksi (345 MPa) yield strength was defined for input to the model of tie bars. The DYWIDAG post-tension bars that tied the walls' respective footing to the lab strong floor were modeled using similar beam elements but without coupling and contact with the footing concrete. The concrete foundation, concrete strong floor, steel tab and steel annular ring were all modeled using eight-node solid elements with reduced integration and hourglass control. The strong floor was not replicated explicitly but modeled as being relatively rigid by a layer of solid elements fully fixed at their base. The steel stiffener plates (see Fig. 4) were modeled using four-node fully integrated shell elements. The shell elements of the stiffener plates were coupled with the solid elements of the annular rings, and with the shell elements of HSS.

Note that the aforementioned mesh sizes of the infill concrete and the steel plates were selected based on the results of a mesh convergence study. To account for the fabrication tolerances of steel in the model, as commonly done in buckling analyses that perform equilibrium in the deformed configuration, the geometry of the web plate and HSS was modified around the bottom region of the wall that covers a height between the second row of the bars and the top of the foundation to include initial imperfection that assumes a sinusoidal shape with a maximum amplitude of 0.01 in (0.25 mm), and wavelength of 2 in (50.8 mm). Shell elements for the steel skin were refined at the bottom third of the wall height by reducing the element height by half.

The numerical solution was carried out using the non-linear static implicit solution procedure of LS-DYNA which is faster compared to the explicit solution and deemed better considering the size of the numerical models (for example, a typical implicit analysis of the NB1 wall model that had 80,670 elements (i.e., 69,628 solids, 9928 shells and 1114 beams) took 60 h using 12-core dedicated processors). To expedite the run time of the numerical models, only one half of the specimen was modeled, taking advantage of the plane of the symmetry of the specimen. The numerical simulation also followed the experimental loading protocol, but applying only one cycle per drift amplitudes as opposed to the three cycles per drift amplitude applied in the tests. In the numerical analysis, the step size of the wall's lateral displacement was selected until a reasonable convergence in the results was obtained. The models were subjected to horizontal cyclic displacements at the top of the wall, in the direction parallel to the plane of the wall. Fig. 7 shows a representative displacement loading history and the step size for the CFSSP-B1 model as a function of time defined in LS-DYNA for the cyclic simulation specified by the user. In the first few cycles, when the wall model is expected to exhibit elastic behavior large step sizes are used to reduce the run time of the simulation. For example, between the 0.44 and -0.44% drift ratio (within the 1 s intervals between 2.5 s. and 3.5 s.) 20 steps at 0.05 s are used; when the model is expected to exhibit inelastic

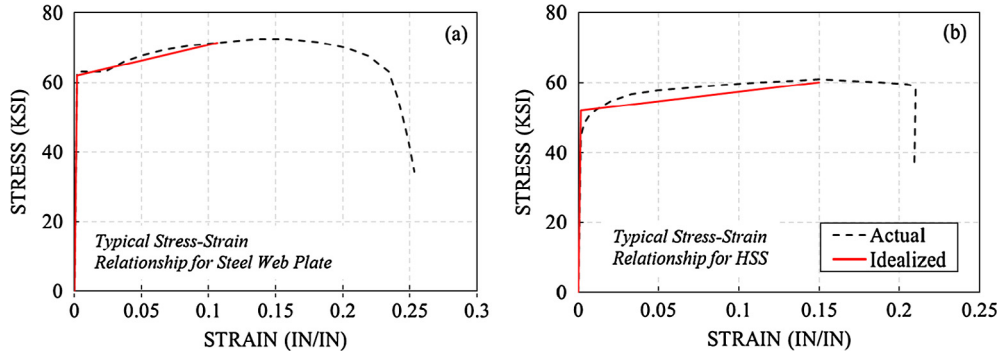

Fig. 6. Typical uniaxial stress-strain relationships with respective idealized steel material models used in LS-DYNA: (a) Web Plate; (b) HSS.

Table 2
Material properties of CFSSP-Walls.

CFSSP MODEL	Average web plate yield strength (ksi)	Average HSS yield strength (ksi)	Average concrete compressive strength (ksi)
B1	62	46	7.1
B2	64	44	4.8
NB1	61	44	6.9
NB2	63	42	6.8

behavior, the time step was reduced to increase the converge of the numerical solution.

3.2. Interface contact and boundary conditions

Initial simulations of the CFSSP-Walls in LS-DYNA were performed using the *automatic_surface_to_surface* contact model which has been used in the LS-DYNA simulation of the steel-plate concrete (SC) composite shear walls by other researchers [13,14]. However, at larger wall deformations, cyclic simulations of the CFSSP-Walls using this contact model with the program default contact stiffness (and using interface friction coefficient of 0.3 or larger) exhibited significant slippage of the concrete inside the HSS in the B models. Such behavior had not been observed in the tests; in other words, the simulations using this contact model gave results inconsistent with the observed physical behavior of the model. Note that the so-called penalty-based method was used (program default method in the contact model definition) for calculating the contact forces. In this method, a force proportional to the amount of penetration is applied between the penetrating node and the opposing surface [15]. This is tantamount to having linear, compression-only springs in the normal direction to resist penetration. However, using the *automatic_surface_to_surface* model, running the same simulations with increased contact stiffness did not eliminate the slippage problem.

To resolve this problem, the interaction between the steel sandwich panels and the infill concrete as well as the interaction between the foundation, the strong floor and the wall was defined using the *automatic_surface_to_surface_mortar* contact model, which is a segment-to-segment penalty based contact, and may provide more accurate results for contacts with higher order elements [15]. (Both models are penalty based, which is basically a slave-node master-surface interaction where a force proportional to slave-node penetration on the master-surface is created, which is tantamount to inserting a compression spring with a particular stiffness between the surfaces). It is also stated in LS-DYNA's user manual [15] that the mortar contact is intended, in particular, for implicit analysis, and, recommended for implicit solution [16]. In the simulations, this contact model was used with the static interface friction coefficient of 0.3 (this contact model uses an isotropic Coulomb friction law [17]), and increased contact stiffness. However, using this contact model with the program default contact stiffness, slippage of the concrete core under large deformation still occurred, but could be eliminated by increasing the contact stiffness.

Fig. 8 shows the comparison of the lateral force-deformation loops obtained from the cyclic simulations of the CFSSP-B1 model using these two contact models using LS-DYNA. Even though the difference in the hysteretic loops may seem subtle, the wall model with the *automatic_surface_to_surface* is shown to exhibit lower ultimate flexural strength (due to the concrete core slippage) to that of the model with the *automatic_surface_to_surface_mortar* contact. Note that for the NB models, the results were not significantly affected by the program contact stiffness parameter (and therefore by the contact models) mainly because, in that case, the concrete infill is continuous and concrete-to-steel interaction is mainly achieved by shear ties.

Note that the degree of the increase of the contact stiffness was determined by analyzing a fixed base CFSSP B1 wall model, and gradually increasing the default penalty stiffness (*SFS, SFM* in LS-DYNA) parameters in the contact model definition. The contact stiffness was increased from the default, *SFS* = 1, by a factor of 3, 5 and 10. Fig. 9 presents the resulting pushover curves. The model with the default contact stiffness exhibited strength degradation at some point during lateral deformation (see Fig. 9) due to slippage of the concrete core. Under increased contact stiffness (*SFS* = *SFM* = 3, 5) the strength degradation of the wall was delayed gradually but not totally eliminated. The slippage of the concrete core (thereby strength degradation) was totally eliminated by having the default contact stiffness at least ten times higher than the program default. Therefore, in the subsequent analyses the contact stiffness was increased to avoid slippage of the concrete core in the simulations.

4. Simulation results

Recall that the objective of this study was to use finite element models to capture the behavior of the tested specimens in terms of initial elastic stiffness, peak strength reach at each displacement amplitude, and pinching behavior during cyclic inelastic behavior. Fig. 10 compares the wall base shear (lateral force) versus drift ratio obtained using LS-DYNA with the experimentally measured values. Fig. 11 compares the LS-DYNA axial strain distribution in the steel skin with the experimentally measured ones along the depth of the cross-section.

Visually, as a first impression, in both cases, the results show a good agreement, particularly in terms of the ability of the model to replicate pinching in the hysteretic loops. Quantitatively, the finite element analyses were able to approximately replicate the maximum measured strength of the tested specimens, and their initial elastic stiffness. For example, the maximum flexural strength

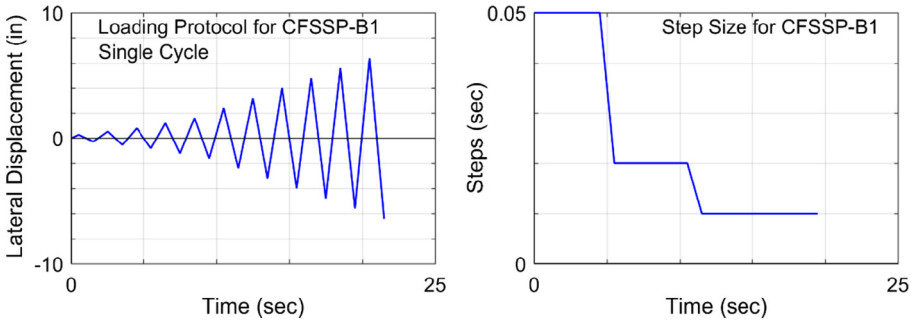

Fig. 7. Displacement loading history and time step size used in the finite element analysis of the wall model for CFSSP-B1.

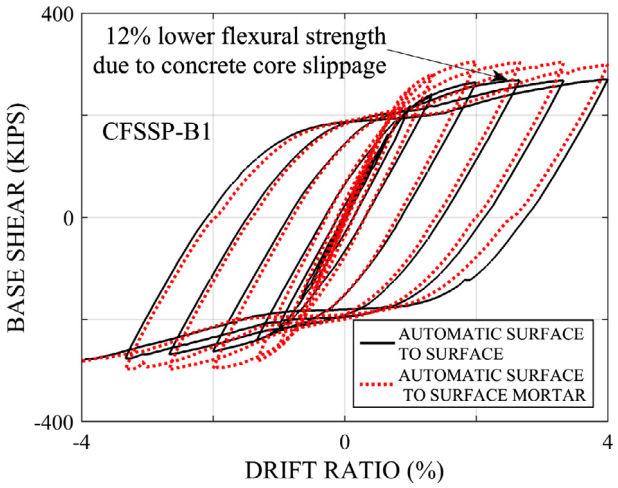

Fig. 8. Comparison of hysteresis loops of the LS-DYNA models for the CFSSP-B1 wall using two different contact models.

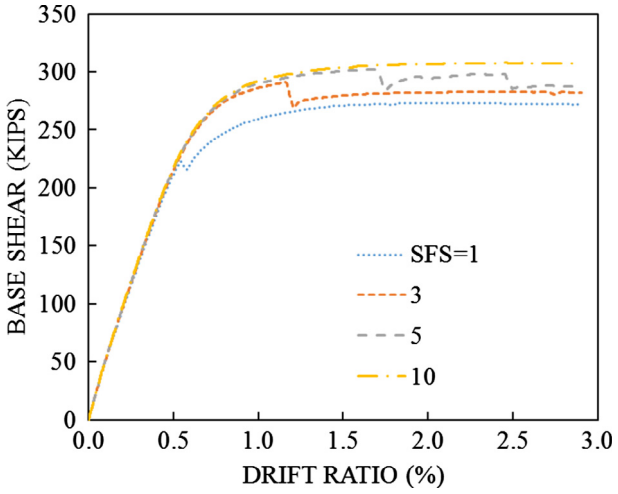

Fig. 9. Effect of increased contact stiffness on the pushover curves of the fixed-base CFSSP-B1 wall model in LS-DYNA.

obtained using LS-DYNA models for the CFSSP-B1 specimen is 108% of the values attained in the test; it is 102%, 101% and 106% respectively for, CFSSP-B2, NB1 and NB2 specimens. Table 3 presents a summary of these results, together with a comparison of the analytically obtained maximum flexural strengths divided by the walls' respective plastic moment.

It was observed that variability in the value of the elastic modulus of concrete has an effect on the initial stiffness part of the model response. Simulations using values of the concrete modulus ranging between 0.5 and 1.0 of the value given by the ACI [9] equation for E_c (presented earlier) showed that $0.5E_c$ gives the best agreement with regards to initial stiffness of the four specimens (for the NB1 model it was slightly underestimated, but good agreements were obtained for all others). Note that the concrete used for the wall specimens (except for specimen B2) had uniaxial cylinder compressive strengths higher than 6000 psi (41.4 MPa). For concrete compressive strengths in excess of 6000 psi (41.4 MPa), the above ACI equation overestimates the modulus of elasticity of concrete [18,19]. Using the alternative equation proposed by ACI [20] for such high strength concrete ($E_c = 40000\sqrt{f'_c} + 1 \cdot 10^6 psi$) gives a value that is 10% less. Given that the ACI equations for the modulus of elasticity of concrete are obtained by regression analysis through data having large scatter, and given that the concrete modulus from cylinder tests was unfortunately not measured during the experiments, it was deemed possible that the specimen had a modulus of $0.5E_c$. Note that steel skin axial strain response was shown to correlate well with the experimental measured data (as presented in Fig. 11), which indicate that curvature was well captured. Having a model that captures the wall curvature right with a different elastic modulus value than that given by the ACI equation indicates that stiffness-related issues depend on the concrete rather than steel skin. To prevent similar calibration issues and uncertainties related to the elastic modulus of the concrete in future studies, it is recommended that the strains on the concrete specimen be also measured. However, for the investigated concepts in this paper, considering concrete with half of its elastic modulus only has an impact on original stiffness, and is not significant otherwise (considering that for CFSSP-Walls, 80% of the flexure is resisted by the steel plates, and concrete serves primarily to prevent plate buckling).

Maximum buckling of the steel skin in the finite element analyses occurred between the first and second row of tie bars, consistently with the experimental observations. Fig. 12 shows the maximum amplitude of the buckling wave of the steel skin obtained using LS-DYNA models, at different positive peak drift locations. Note that models B2 and NB2 (that have tie spacing-to-thickness ratio of $S/t = 38.4$) exhibit a greater amplitude of buckling at a given drift than their corresponding models B1 and NB1 (that have a tighter tie spacing-to-thickness ratio of $S/t = 25.6$).

Figs. 13 and 14 illustrate the stress-strain history of the steel-skin at various points along the depth of the cross section (note that the depth of the cross-section is expressed in the global X direction with a centroid located in the middle of the cross-section), obtained from the cyclic finite element analyses of the B and NB walls. The wall heights at which these relationships are reported are the same as those where actual strain measurement were obtained in testing (i.e., at 10 in (254 mm) and 16 in (406.4 mm) for B1 and NB1). The peak positive drift locations for each loading cycle are marked in the figures using numbers from 1 to 9, where one stands for the first drift amplitude level (i.e., 0.27% drift ratio for Group B Walls and 0.20% drift ratio for Group NB Walls) and nine stands for the ninth one (i.e., 4.00% drift ratio for Group B Walls and 3.60% drift ratio for Group NB Walls) in the loading protocol. The stress strain history of the steel skin indicates that yielding starts at 0.67% drift ratio (cycle number 3) in the outermost steel elements for CFSSP-B1 (Fig. 13(a)), and at 0.90% drift ratio for CFSSP-NB1 (Fig. 14(a)); as expected, in regions close to wall centroid, yielding only started at higher drift levels. For example, for CFSSP-B1 (Fig. 13(a)), at the cross-section depth of X = −9.4 in (238.76 mm) (steel plate is in tension), yielding started at about a drift ratio of 1.33% (cycle number 5), whereas at the depth of X = 21.8 in (553.72 mm), it started at about 0.90% drift ratio.

The simulation results were used to check the adequacy of the design approach used to determine the amount of connector re-bars (running through the web of the wall) required to transfer the in-plane wall shear and moment forces to the foundation footing. Note that in the design of the connector re-bars, a conservative (lower-bound) approach was adopted in which the web plates were assumed to reach their yield strength, and the tension forces corresponding to the fully yielded steel parts of the wall (assumed conservatively as $1.5F_y h t_w$, where t_w and h, are the web thickness and width tributary to the connector re-bars) that were assumed to be transferred to the footing using three rows of re-bars located in the bottom part of the wall embedded in the foundation. Design shear strengths of re-bars were calculated using the equation for the strength of a stud as reported in [1].

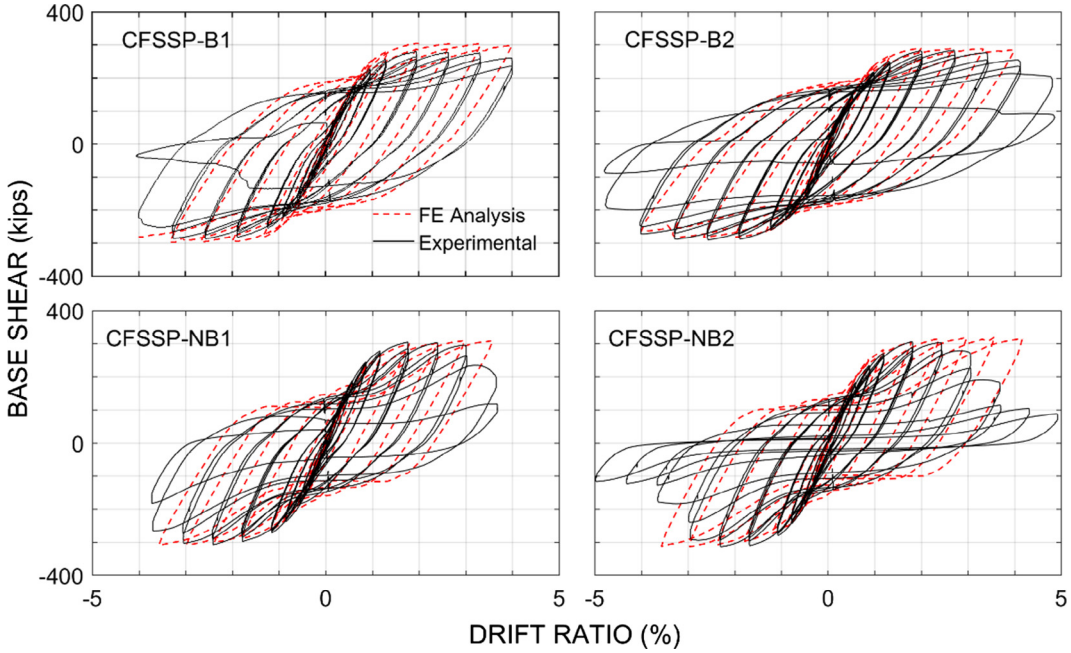

Fig. 10. Comparison of the hysteresis curves of the LS-DYNA models and the tested specimens of the CFSSP-Walls.

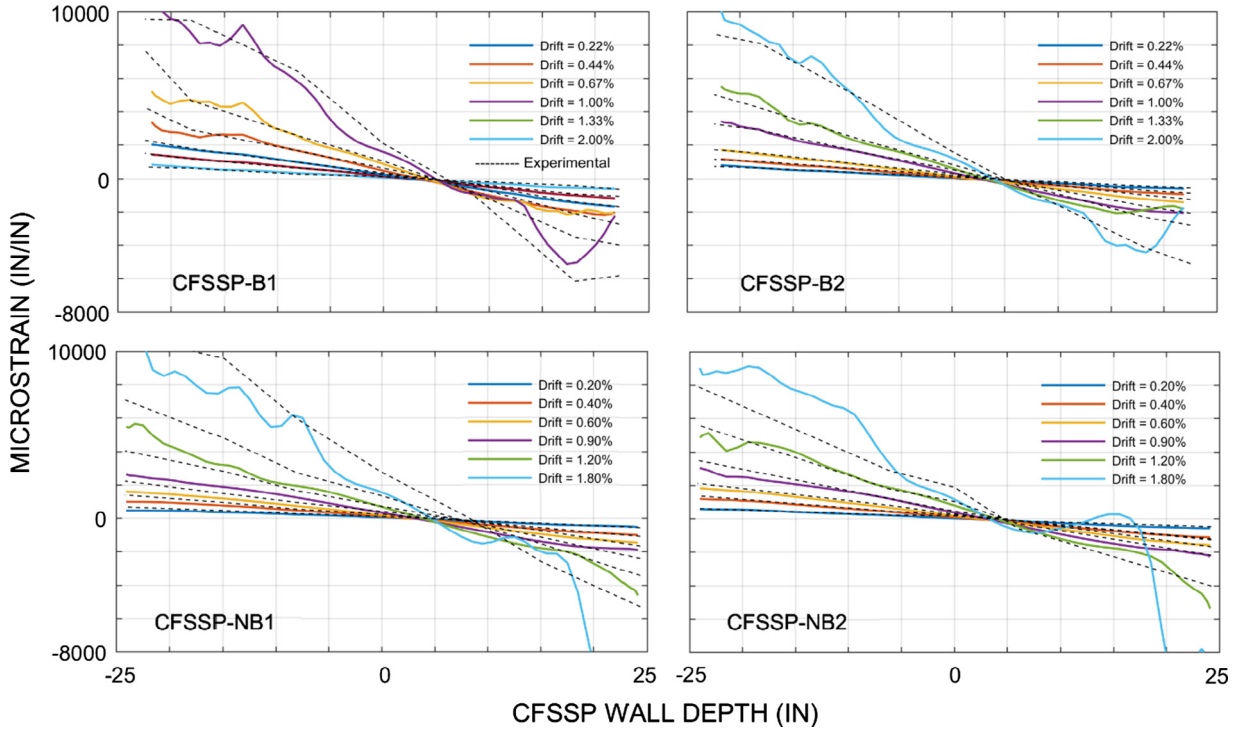

Fig. 11. Comparison of the strain distribution of the LS-DYNA models and the tested specimens of the CFSSP-Walls along the depth of the cross-section (values changing from 2.00% to 0.22% drift and 1.80% to 0.20%drift from top to bottom).

However, finite element simulations indicate that the force distribution inside the wall footing is rather complex. The embedded part of the wall is subjected to both shear and moment forces under wall lateral displacement. These forces are transferred to the foundation footing via shear forces on the connector re-bars, bearing forces on the circular rings and on the other contact surfaces of the wall. Fig. 15 illustrates the embedded part of the wall inside the footing of the half symmetric NB1 model. The figure displays the internal and the external forces (internal forces are given by the normal and shear stresses, and external forces are given by the nodal reaction forces) under positive lateral wall deformation and illustrates the compression zones (shaded areas) created under wall deformation due to flexural deformation and bearing forces of contacted interfaces. In the illustration, tensile, compressive and shear forces are denoted by *T*, *C* and *V*, respectively; the total nodal reaction forces are denoted by *N* (for nodes

Table 3
Comparison of experimental and finite element results.

	CFSSP-B1	CFSSP-B2	CFSSP-NB1	CFSSP-NB2
Test Peak Load (kips)	281	283	305	302
F.E. Peak Load (kips)	305	289	309	320
F.E./Test	1.08	1.02	1.01	1.06
M_p (kip-in)	28517	26677	32317	31272
F.E. Max. Moment (kip-in)	36600	34680	37080	38400
M_{max}/M_p	1.28	1.30	1.15	1.23

F.E: Finite Element

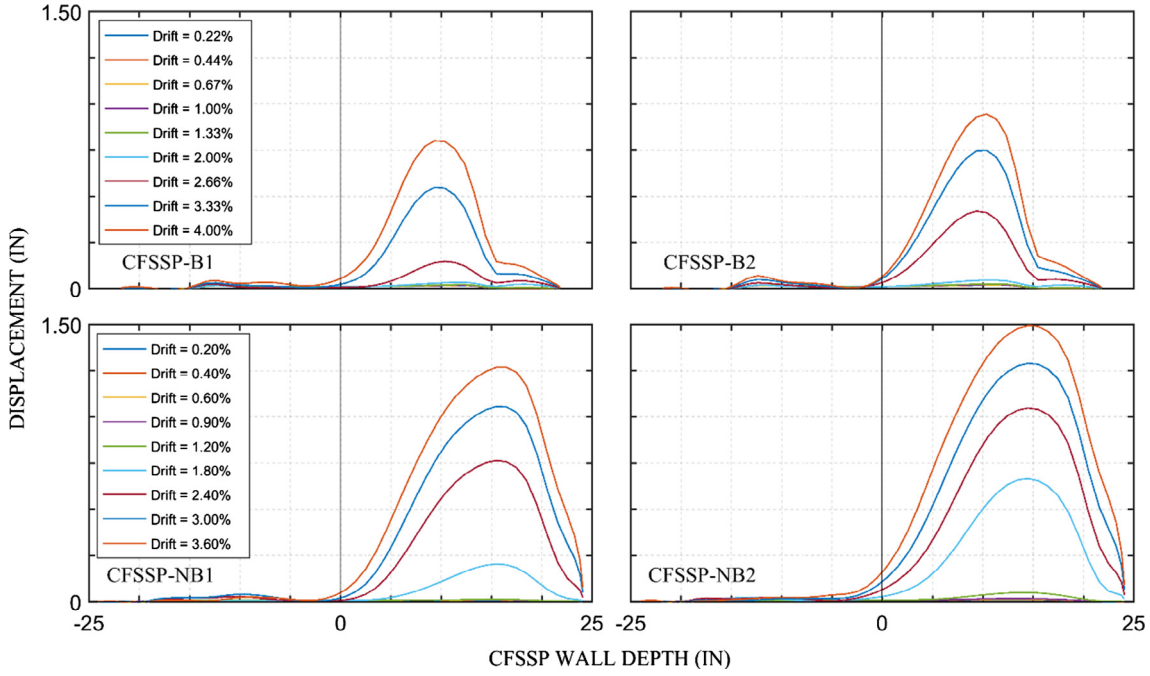

Fig. 12. Amplitude of buckling wave of the steel skin of the LS-DYNA models of the CFSSP-Walls (values changing from 3.60% to 0.20% drift, and 4.00% to 0.22% drift from top to bottom).

that are located at the contact interface); the subscripts refer to the name of the parts considered ($_{SS}$: steel skin, $_C$: concrete, $_{rbH}$: re-bar horizontal, $_{rbV}$: re-bar vertical, $_{RR}$: right ring, $_{LR}$: left ring, $_{HSS\text{-}R}$: HSS right, $_{HSS\text{-}L}$: HSS left). Equilibrium of vertical forces is given by the relationship:

$$T_{SS} + N_C + N_{RR} + N_{HSS-R} = V_{rbV} + C_{SS} + C_C + N_{LR} + N_{HSS-L} \quad (1)$$

Equilibrium of the horizontal forces is given by the relationship:

$$V_{SS} + V_C + N_{HSS-L} + N_{LR} + N_C + N_{RR} = V_{rbH} + N_{HSS} \quad (2)$$

For example, pushover analysis of the CFSSP-NB1 wall resulted in the following vertical forces at 2.5% drift ratio: T_{SS} = 671 kips (2985 kN), N_{CC} = 162 kips (721 kN), N_{RR} = 260 kips (1157 kN), $N_{HSS\text{-}R}$ = 50 kips (222 kN), V_{rbV} = 218 kips (970 kN), C_{SS} = 337 kips (1499 kN), C_C = 330 kips (1468 kN), N_{LR} = 250 kips (1112 kN), $N_{HSS\text{-}L}$ = 27 kips (120 kN). Results showed that the re-bars transfer roughly 40% of the tensile forces due to yielding of the steel web plate; hence, the simplified design procedure proved to be satisfactory.

The simulation results were also used to measure the force demand on the bottom rows of tie bars under cyclic wall loading, and check if these tie bars remained elastic as intended. Note that the diameter of the tie bars should be selected such that they can provide adequate stiffness to control local buckling of the web plates, resist the shearing force transferred between the infill concrete and the steel skin plate, and have adequate strength to resist the tensile force that develops during formation of the plastic mechanism created during inelastic buckling of the web steel plate [1,2]. Previous study on flexure dominated CFSSP-Walls by Eom et al. (2009) showed that crushing of the concrete and tie bar fracture following steel plate buckling was reported to cause the failure of the walls. Furthermore, at the time the walls were tested, there were no guidelines on how to design tie bars for the CFSSP-Walls. Note that, CFSSP-Walls had no tie bar fracture but a weld-connection fracture that propagated into steel plate. Because the weld-fracture phenomenon is neglected in the finite element models, the behavior of the ties is observed even at large drifts which otherwise could not be seen in testing due to welding fracture.

The tie bar diameter used in the studied specimens is greater than the diameter predicted by the theory presented in [1] (and developed after the tests) that assumes a design shear force stemming from the plastic hinge formation of the buckled plate as explained in [1]. For the specimens, 1 in (25.4 mm) diameter ties were used throughout, with theoretical shear and axial yield strengths of 24 kips (106 kN) and 39 kips (173 kN), respectively. Focusing on the finite element analysis results for the NB1 model, Fig. 16 shows the horizontal and vertical shear forces transferred between the infill concrete and the steel skin plate, and the axial force demand of the tie bars, for tie bars located in the first and

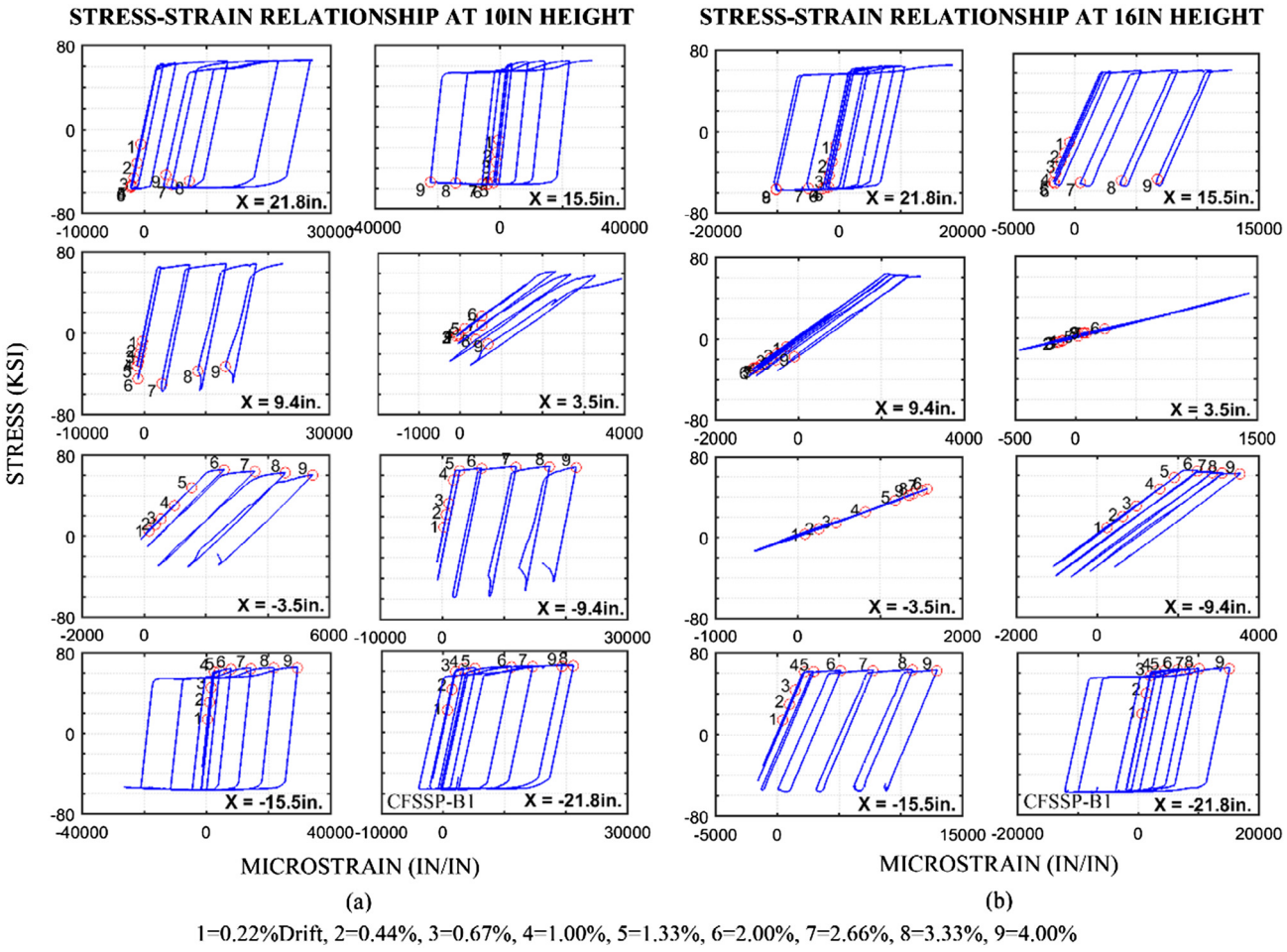

Fig. 13. Stress-strain relationship of steel skin of the LS-DYNA model of CFSSP-B1 along the cross-section depth: (a) stress-strain relationship at 10 in; (b) stress-strain relationship at 16in (1 = 0.22%, 2 = 0.44%, 3 = 0.67%, 4 = 1.00%, 5 = 1.33%, 6 = 2.00%, 7 = 2.66%, 8 = 3.33%, 9 = 4.00% drift).

second rows of ties along the wall depth, at each positive peak drift of the cyclic loading. Note that the trend in demands changes when local buckling develops, which the finite element analyses show occurs starting at 1.20% drift ratio for the NB1 model (see Fig. 12); before local buckling, maximum shear forces in these tie bars are less than 10 kips (44 kN). After buckling, results indicate that the tie shear forces reached 23 kips (102 kN) vertically and 10 (44 kN) kips horizontally in those ties located above and below the buckling wave of the steel plate (on the compression side), while axial forces reached 15 kips (66 kN). Comparing those numbers to the 24 kips (106 kN) and 39 kips (173 kN) shear and axial yield strengths of the tie bars shows that the tie bars almost yielded in shear. Note that for the B models (results not shown), these forces are much lower; for instance, the total horizontal force in the first row of ties is about 30 kips (133 kN) for the NB1 model at 3.60% drift ratio, and but only about 5 kips (22 kN) for the B1 model at 4.0% drift ratio. The shear and axial force distribution of the critical tie bars obtained computationally in the research presented here showed that governing shear forces occur in the form of vertical shear following steel plate buckling which could not be predicted by the theoretical design.

5. Plastic strain for fracture

Effective plastic strain contours of the steel skin from the finite element simulations (not shown here due to space limitations) of the B models indicate that (as expected) the highest values of plastic strains form at the middle of the buckled wave of HSS (i.e., between the top of the footing and the first row of ties, at a wall height of 2 in (50.8 mm) from the footing). This behavior is consistent with the test observation made for specimen B2, as cracking was initiated there; note that, for that specimen, it also simultaneously initiated in the web-plate around some of the plug-welds or fillet welds of the tie (as described in [1,2]). On that latter point, modeling initiation and propagation of the cracks around the tie bars is beyond the scope of this work as it would require meshing strategies and material modeling approaches much different than those reported above. However, while it is recognized that propagation of the cracks that have initiated around ties in the web plate will have an impact on strength degradation, as far as cracks in the HSS are concerned, the ability to determine the cumulative plastic stains at crack initiation at that location is useful to determine the onset of strength degradation (even though the rapidity of this degradation may not be accurately modeled). Such cumulative plastic strains in the steel of the NB and B specimens are shown in Fig. 17 at various wall drift levels. Fig. 17 shows the maximum effective plastic strain distributions (maximum values of the three integration points located through shell thickness) at each positive peak drift of the loading cycle along the half wall depth (they are approximately symmetric on the other side of the wall depth) for the B and NB models obtained using the LS-DYNA simulations. These values are reported at the wall height where they were indicated to be highest (2 in (173 mm) for the B models, and 8 in

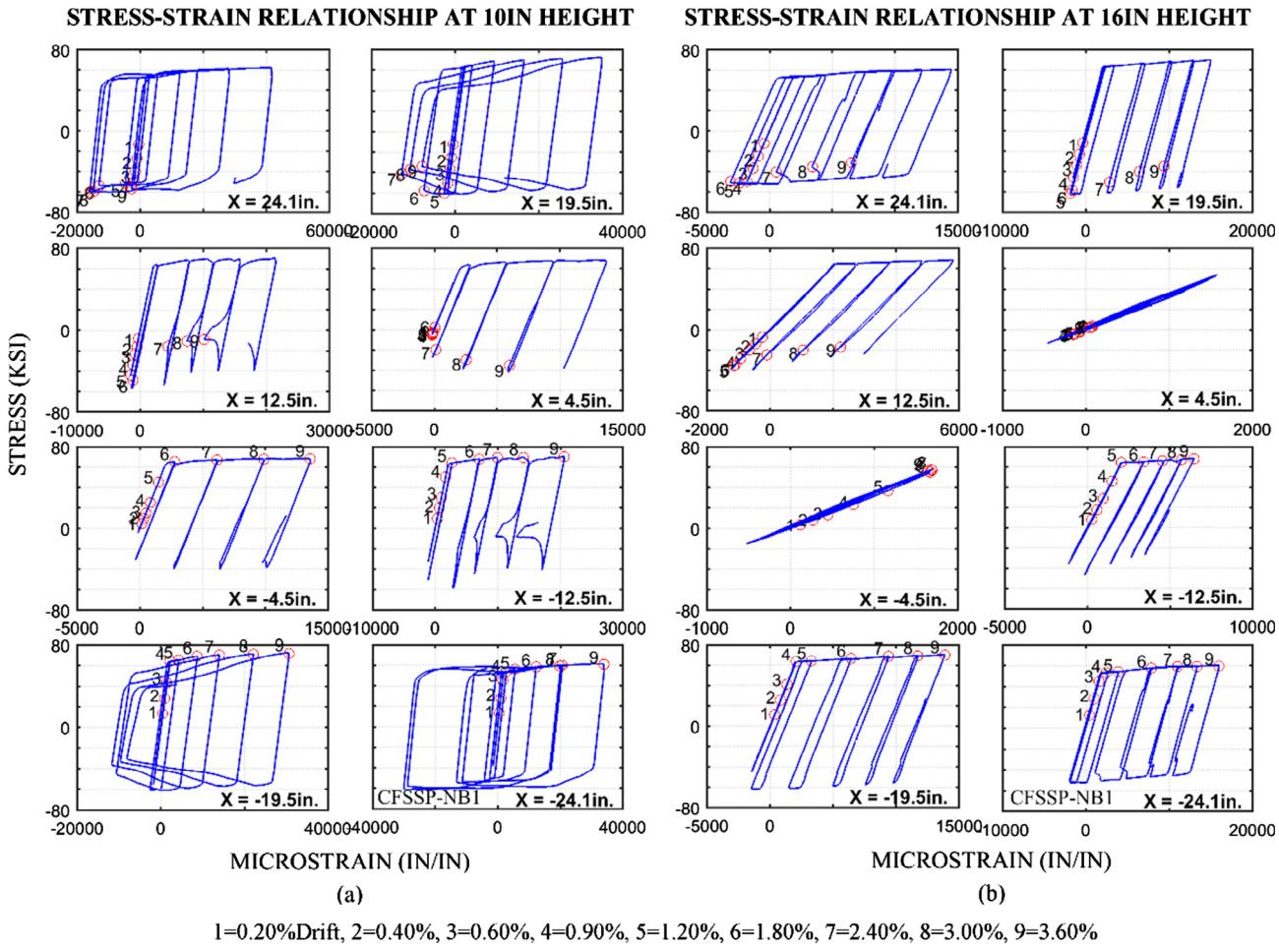

Fig. 14. Stress-strain relationship of steel skin of the LS-DYNA model of CFSSP-NB1 along the cross-section depth: (a) stress-strain relationship at 10 in; (b) stress-strain relationship at 16in (1 = 0.20%, 2 = 0.40%, 3 = 0.60%, 4 = 0.90%, 5 = 1.20%, 6 = 1.80%, 7 = 2.40%, 8 = 3.00%, 9 = 3.60% drift).

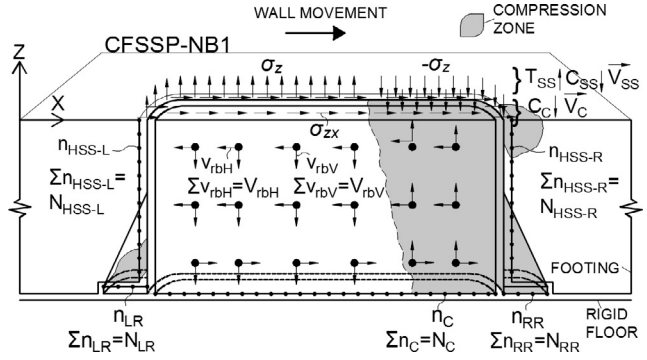

Fig. 15. In-plane shear and moment force transfer in the wall footing of the LS-DYNA model of CFSSP-NB1.

(203.2 mm) for the NB models). These curves indicate that strains are highest at the wall ends, and they are used to determine the failure strains for the shell elements of the HSS in the damage model simulations.

Table 4 shows the maximum of plastic strain values at the outermost HSS element of the B2 model for all the simulation cycles. For the B2 wall, strength degradation occurred at the wall drift ratio of 4.67%. Repeated simulations indicated that, in order to simulate such behavior, using cumulative plastic strain at failure higher than the one at 4.00% drift ratio can reasonably replicate global strength degradation of the model (in this case a failure strain within a range of ~1.40–1.45). Table 4 also shows the corrected cumulative plastic strain values for the actual specimen obtained by modifying the values corresponding to the finite element with one cycle at each target drift to match the experimental case which had more cycles at each target drift. Assuming that fracture on the HSS will occur after 4.00% drift ratio, the corrected cumulative failure strain is obtained as 2.60. The effect of steel fracture on the HSS cyclic response is illustrated in Fig. 18 for the NB1 model for a failure strain of 1.0 determined using a similar approach as described above for the B2 model.

6. Stress analysis of steel skin and infill concrete

In this section, the distribution of shear and normal stresses along the cross section of steel skin and the concrete infill, and the interaction of horizontal uniaxial stresses and shear stresses on the vertical uniaxial stress (per Von Mises yield criteria), as obtained from the LS-DYNA models, is investigated. Note that because of the circular shape of the boundary elements in this cross-section (see Fig. 4), the shell stresses in the steel section of the model are reported in local coordinates. Fig. 19 illustrates the shell local coordinate used in the LS-DYNA models in conjunction with the global coordinate system. Note that local Y-axis of shell elements is parallel to the global Z-axis, and through the thickness coordinate of the shell element is given by its local Z-axis. The stresses in the solid elements of the infill concrete are directly reported in the global coordinate system.

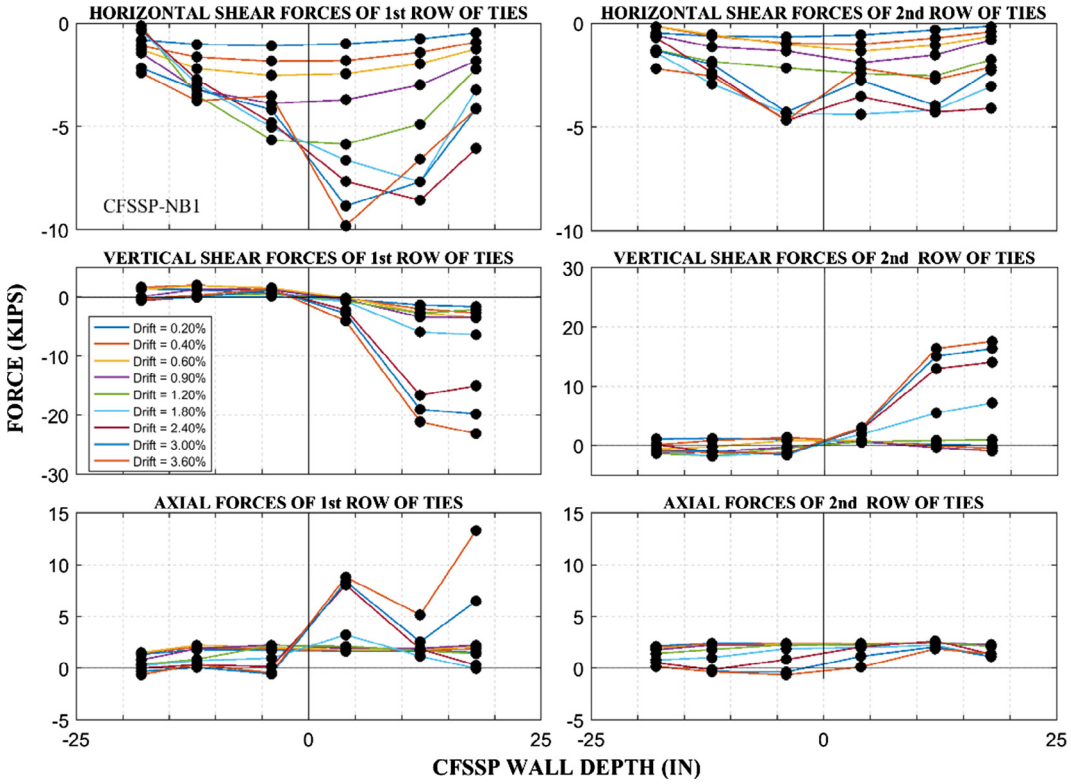

Fig. 16. Shear and axial forces of the 1st and 2nd row of ties of the LS-DYNA model of CFSSP-NB1 at positive peak drifts (values changing from 3.60% to 0.20% drift from top to bottom).

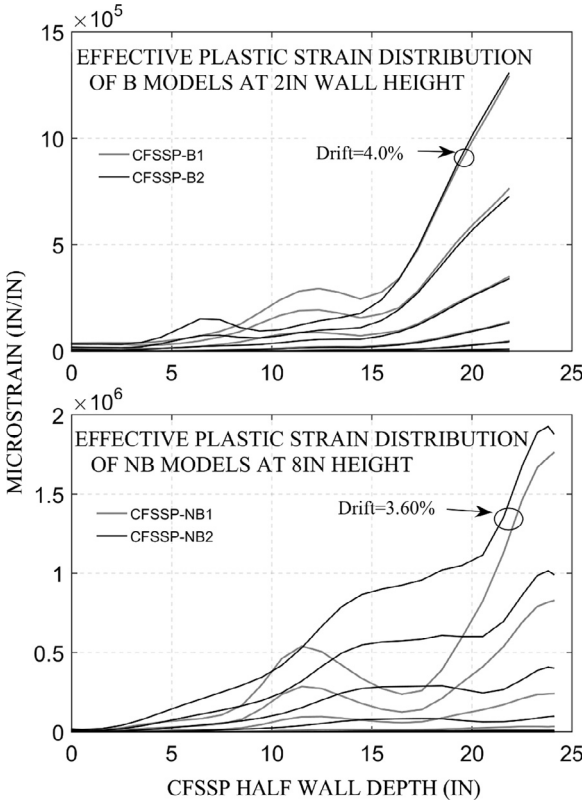

Fig. 17. Effective plastic strain distribution along the half wall depth of CFSSP-Wall models obtained using LS-DYNA.

The steel material used in the LS-DYNA models uses the Von Mises yield criterion which is expressed in terms of three-dimensional normal and shear stresses as follows:

$$\sigma_{VM} = \frac{1}{\sqrt{2}}[(\sigma_x - \sigma_y)^2 + (\sigma_y - \sigma_z)^2 + (\sigma_z - \sigma_x)^2 + 6(\sigma_{xy}^2 + \sigma_{yz}^2 + \sigma_{zx}^2)]^{\frac{1}{2}} \quad (3)$$

where σ_x, σ_y, σ_z are normal stresses and σ_{xy}, σ_{yz}, σ_{zx} are shear stresses in a three-dimensional continuum body. For the work presented in this paper, presentation of the stress components in two dimensions (i.e., for shell elements, locals stresses: σ_x, σ_y and σ_{xy}; and for solid elements, stresses: σ_z, σ_{yz} and σ_{zx}) were deemed to be sufficient to illustrate the distribution of forces throughout the cross-section.

Figs. 20 and 21 illustrate the distribution of the shear and normal stresses across the depth of the cross-section in the steel skin and concrete infill at the wall base Note that these stresses were read at 1 in (25.4 mm) about the footing in the LS-DYNA models to avoid stress concentration effects due to localized bearing pressures of the wall on its footing. For reasons described above, the shell stresses shown in Figs. 20(a) and 21(a) are in local coordinates, whereas solid stresses shown in Figs. 20(b) and 21(b) are in global coordinates. Note that each reported solid stress value is actually the average of the values in the elements located through thickness of the wall model. The stress distributions are reported at the positive peak drift amplitude reached in each cycle, which results in compressive axial stresses (negative in sign) at the outermost positive X location of the cross-section depth, and tension axial stresses (positive in sign) at the outermost negative X location of the cross-section depth. For clarity of description in

Table 4
Effective plastic strain values for the CFSSP-B2 wall model at peak positive drifts.

Drift ratio (CFSSP-B2) (%)	Cycle order (i)	Cycle for each drift (n)	Cumulative plastic strain (PS) LS-DYNA (single cycle)	PS_{i+1}-PS_i	n x PS_{i+1}-PS_i (corrected PS)
0.23	1	3	0	0	0
0.36	2	3	0	0	0
0.56	3	3	0	0	0
1.00	4	3	0.0085	0.0085	0.0255
1.33	5	3	0.0436	0.0351	0.1053
2.00	6	2	0.1321	0.0885	0.177
2.67	7	2	0.3387	0.2066	0.4132
3.33	8	2	0.7248	0.3861	0.7722
4.00	9	2	1.3059	0.5811	1.1622
–	–	*1*	*FS = 1.43*	*0.1241*	*0.1241*
4.67	10	2	NA	NA	NA
					$\sum PS$ = 2.60

Italics and underlined values are corresponding to the cumulative plastic strain value at failure.

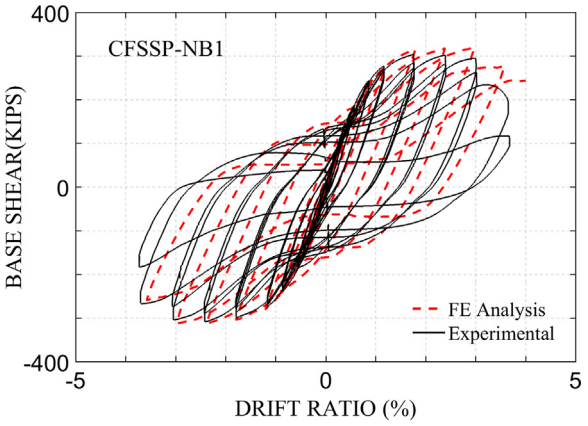

Fig. 18. Resulting hysteresis curve due to HSS fracture.

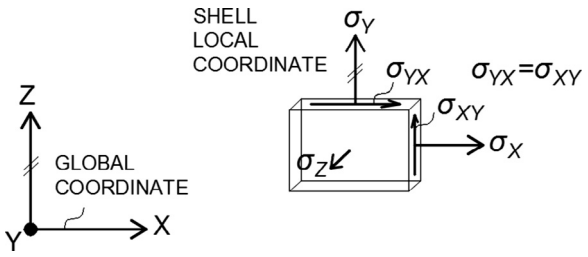

Fig. 19. Local shell coordinate used in the LS-DYNA models.

the following, the tension and compression sides are defined based solely on the axial stresses shown in the figures.

The horizontal normal stress distribution for the steel skin is given by the horizontal shell stress, σ_x. Note that as the steel skin gets in tension vertically, it also tends to compress horizontally due to Poisson's effect. These compression stresses, if free to develop, would reduce the diameter of the circular steel shell at the boundaries of the wall, but because of the presence of the infill concrete within the boundary elements, the steel skin's compressive deformations in the horizontal direction due to Poisson's effect are somehow prevented, which therefore creates relatively high hoop stresses in this region of the wall (see Figs. 20(a) and 21(a)). Under vertical compression, the steel skin tends to uniformly compress at this wall elevation (1 in (25.4 mm)), but at higher wall elevations, in particular at regions where the local buckling of the steel-plate takes place, the distribution of stresses is rather complex; for example, after buckling, the steel skin attains larger horizontal tensile stresses while the vertical stress is significantly reduced. Because of the interaction of the stresses (per Von Mises yield criteria) the vertical uniaxial stress of the steel skin is increased on the tension side but reduced on the compression side of the wall. For example, at 2.66% drift ratio for the B1 model (Fig. 20(a)), the ultimate vertical stress for the HSS on the tension and compression side of the wall is 65.2 ksi (449 MPa) and −53.5 ksi (368 MPa), respectively. Similarly, at 2.40% drift ratio for the NB1 model per (Fig. 21(a)), they are 60.4 ksi (416 MPa) and −49.3 ksi (340 MPa), respectively for the HSS.

The axial stresses of the steel skin (σ_y) and concrete (σ_z) in the figures can be used to verify the elastic and plastic neutral axis locations of the wall models. The plastic neutral axis based on the assumed plastic stress and equations provided in Table 1 are shown in Figs. 20 and 21 by dashed lines and the acronym P.N.A. For example, the location of the P.N.A from the wall centerline is 7.8 in (198.12 mm) and 9.3 in (236.22 mm) for the B1 and NB1 wall models, respectively, with steel strength taken as uniaxial coupon values (equal in tension and compression) and concrete strength taken as uniaxial compressive cylinder strengths, whereas stress distribution in Figs. 20 and 21 show an actual plastic neutral axis at approximately 4 (101.6) to 5 in (127 mm) in both cases. The difference is mainly attributed to the assumption in the shape of the compression block of the concrete and also to the unequal axial stress of the steel skin under tension and compression due to the Von Mises interaction of stresses, as described previously. To quantify this first effect, location of the P.N.A. was recalculated by roughly approximating the stress block of the concrete as triangular (to approximately match the stress distribution observed at 2.0% and 1.8% drift ratios, for B1 and NB1, respectively.) and assuming constant concrete stress block thickness, t_c, such that the resultant compressive force is given by: $C = k_1 k_3 f'_c t_c c$ [18], where $k_1 = 0.5$ (ratio of the average compressive stress to the maximum stress), $k_3 = 1.3$ (ratio of the maximum compression stress to f'_c), and c is the depth of the stress block. The recalculated location of the P.N.A. from the wall centerline (using stress values at 2.0% drift for B1 and 1.8% for NB1) is 5.5 in (139.7 mm) and 6.5 in (165.1 mm) for the B1 and NB1 wall models, with steel strength taken as the values read from Figs. 20 and 21 (unequal in tension and compression). To determine if the inequality in the steel axial yield stress in compression and tension had a large effect on the results recalculation of the P.N.A. locations using the tension yield stress from Figs. 20 and 21 for both tension and compression gave results of 5.90 in (149.8 mm) and 7.20 in (182.8 mm) for B1 and NB1, respectively that indicates insignificant effect on the wall's plastic neutral axis.

The shear stress distribution for the steel skin is given by the local shell stress, σ_{xy}. Note that the integration of these shear stresses (in global coordinate) in the shells and solids over the entire cross-section at the wall base results in the total base shear shown in Fig. 10 (and equal to the lateral force applied at the top of the wall).

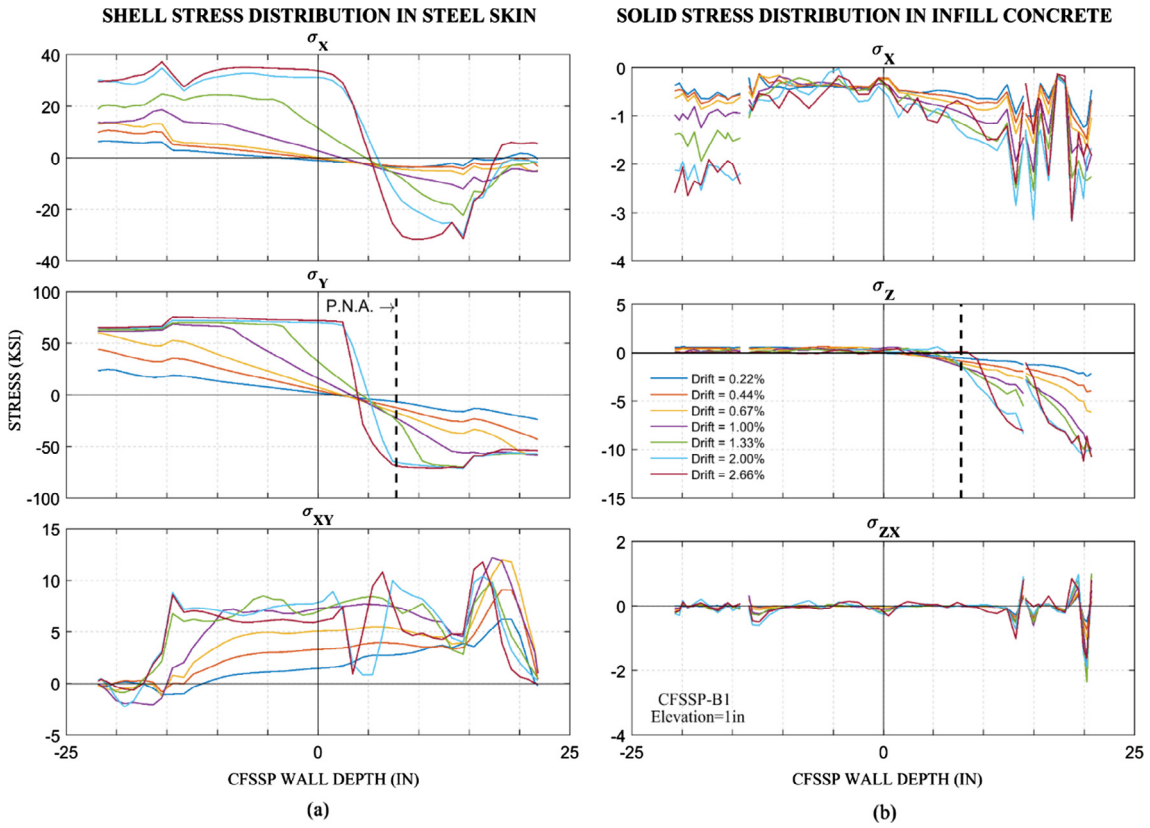

Fig. 20. Plane stress distribution of the cross-section of the LS-DYNA model of CFSSP-B1 located at 1in wall height: (a) Shell stress distribution in steel skin; (b) Average solid stress distribution in concrete (values changing from 2.66% to 0.22% drift from top to bottom).

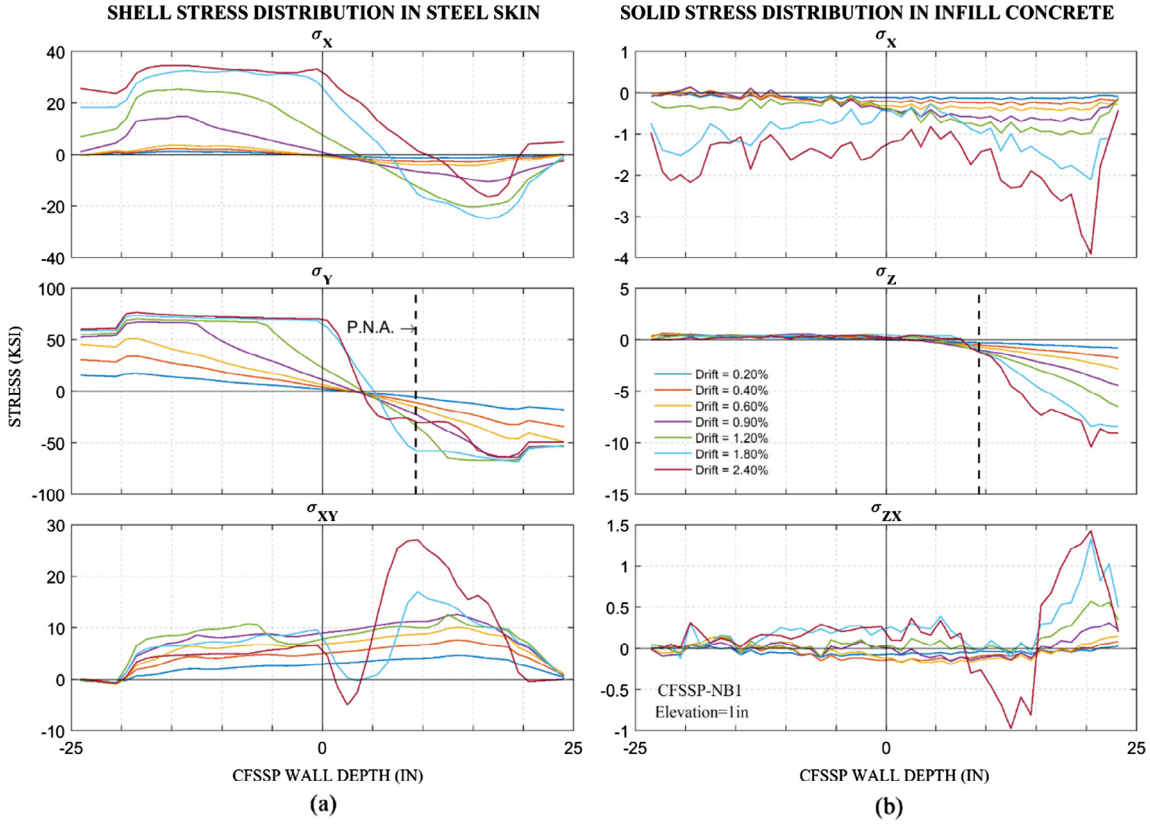

Fig. 21. Plane stress distribution of the cross-section of the LS-DYNA model of CFSSP-NB1 located at 1in wall height: (a) Shell stress distribution in steel skin; (b) Average solid stress distribution in concrete (values changing from 2.40% to 0.20% drift from top to bottom).

The effect of the individual shell stress components on the Von Mises stress of the steel skin is illustrated in Figs. 22 and 23. These figures show the Von Mises stress distribution on the steel skin at the wall base (at 1 in (25.4 mm) elevation) and higher wall elevation (at 10 in (254 mm)), at the peak positive drift reached during each displacement cycle, along the wall depth of the CFSSP-B1 and NB1 wall models, respectively. In these figures the contribution of the three-dimensional stress components (σ_x, σ_y, σ_{xy}) on the Von Mises yielding of the steel skin are shown at randomly selected points along the depth of the wall for different peak drift levels. Note that the axial stress-strain relationship mentioned earlier was used in the definition of the steel material model. Compared to that uniaxial stress value, when the steel skin gets in tension vertically the amount of increase in the wall's vertical axial yield stress, due to horizontal shell tensile stresses (hoop stresses), is observed to be as high as 15%; similarly, when the steel skin gets in compression vertically, the same amount of decrease was observed as shown in Figs. 22 and 23. At regions close to the neutral axis of the wall, shear stresses account for approximately 60% of the uniaxial stress but are significantly less the further away from this neutral axis.

7. Vertical force equilibrium in boundary elements with and without interface friction

It is of interest to investigate the effect of interface friction on the axial force demand on the components of the boundary elements (i.e. HSS and the concrete within HSS), and thereby the vertical force flow between the components of the boundary elements. In the CFSSP-Walls considered herein the composite

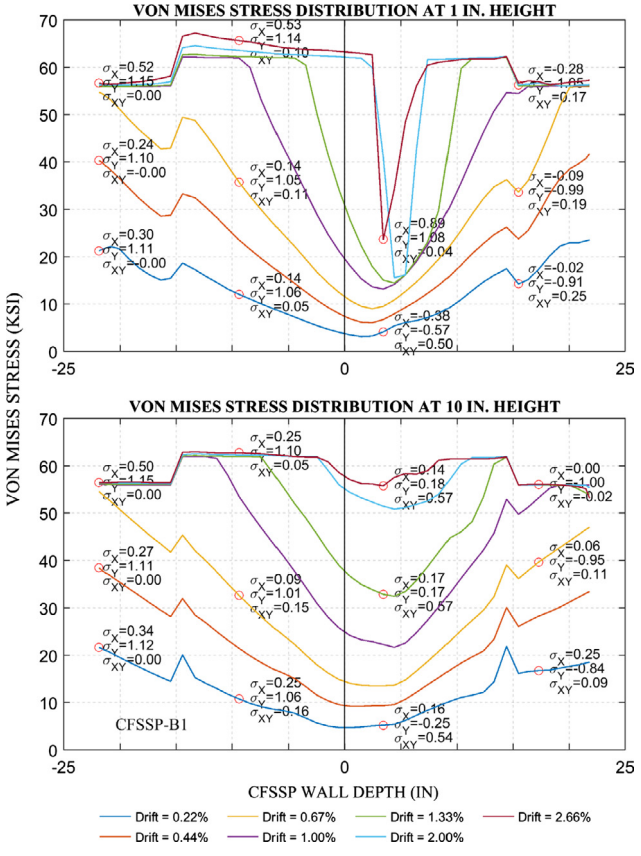

Fig. 22. Von Mises stress distribution along the cross-section depth of the LS-DYNA model of CFSSP-B1 and normal and shear stress contributions (values changing from 2.66% to 0.22% drift from top to bottom).

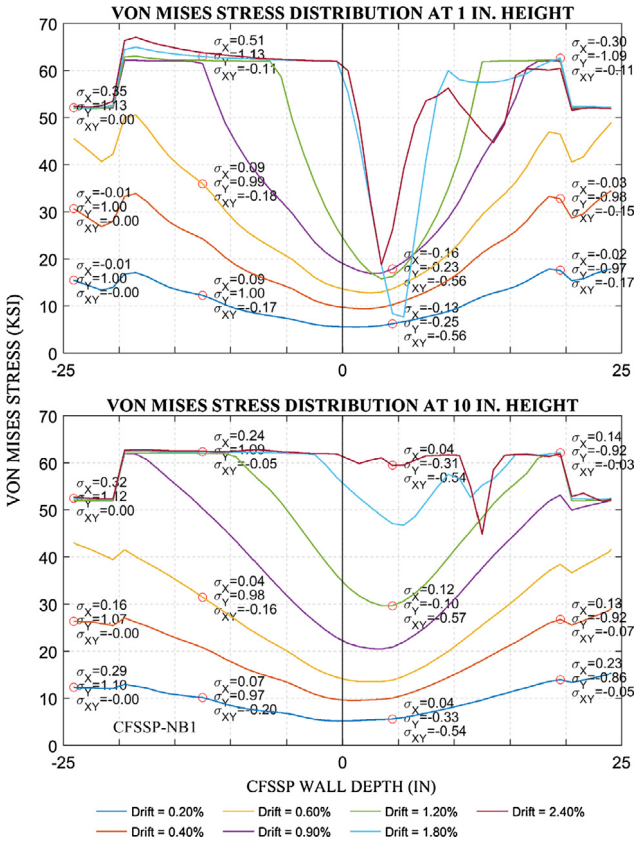

Fig. 23. Von Mises stress distribution along the cross-section depth of the LS-DYNA model of CFSSP-NB1 and normal and shear stress contributions (values changing from 2.40% to 0.20% drift from top to bottom).

action between the concrete (concrete between the steel web plates) and the web plates are mainly accomplished by the row of ties placed along the wall height, and interface friction in this part of the wall is expected to be not substantial, because the normal pressures between these parts are not expected to be significant under in-plane loading of the wall. However, contrary to walls with no boundary elements, CFSSP-Walls have boundary elements in the form of end caps which are subjected to high pressures under in-plane loading of the wall that ultimately creates considerable interface friction between the components of the boundary elements, which plays a significant role in the vertical force distribution for the components of the boundary elements. This may be a central issue particularly for B model, where no ties are used between the HSS and the concrete inside (recall that infill concrete is not continuous), and the composite action is assumed to be accomplished solely by the interface friction between these parts.

Figs. 24 and 25 shows the schematic of a partial section of the half symmetric B and NB model, respectively. Part (a) of the figures illustrates the steel web plate, concrete infill, HSS and concrete core, and parts (b) to (e) illustrate the vertical flow of force on these parts under positive lateral wall deformations. Forces due to internal stresses are denoted by F, nodal reaction forces are denoted by N (for nodes that are located at the interface), and subscripts denote the names of the parts ($_{WP}$: web plate, $_{CI}$: concrete infill, $_{CC}$: concrete core). The nodal reaction forces are the result of contact interface forces and pressures. For example, for the B model, the nodal reaction forces of HSS, N_{HSS}, have contributions from the two contact interfaces; one from the infill concrete between the web plates and the other from the concrete core of the HSS.

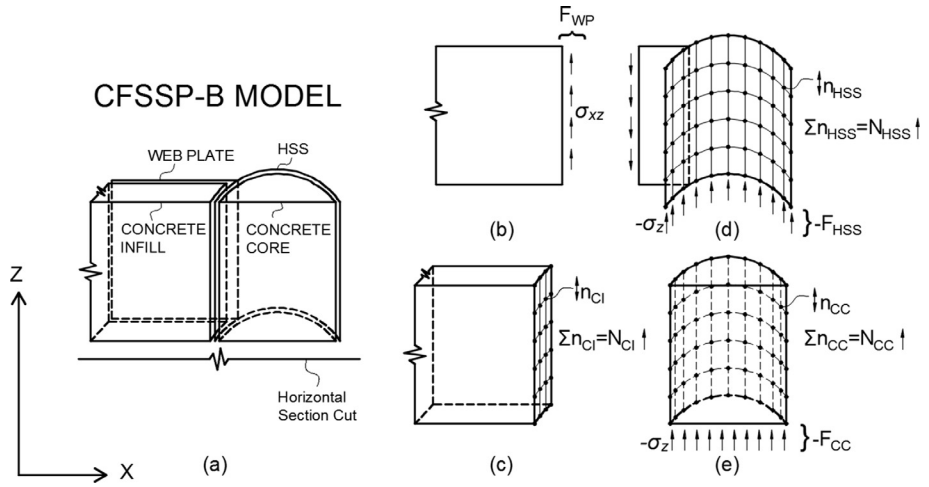

Fig. 24. Vertical force flow on boundary elements of CFSSP B model: (a) web plate, HSS, concrete infill and concrete core of partial wall section; (b) web plate shear force; (c) concrete infill interface nodal force; (d) HSS axial and interface nodal forces; (e) concrete core axial and interface nodal forces.

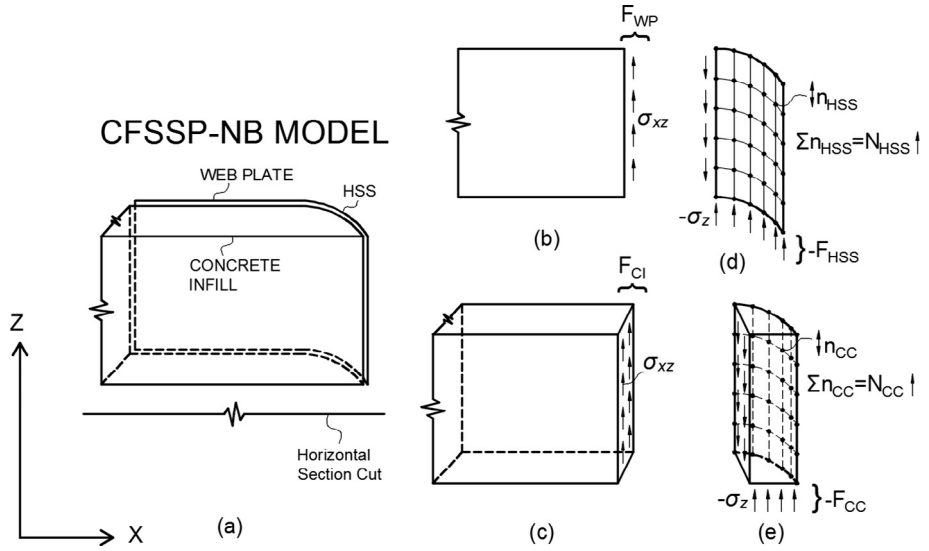

Fig. 25. Vertical force flow on boundary elements of CFSSP NB model: (a) web plate, HSS and concrete infill of partial wall section; (b) web plate shear force; (c) concrete shear force; (d) HSS axial and interface nodal forces; (e) concrete core axial and interface nodal forces.

Under rightward deformation, at the top of the wall the formation of vertical shear forces in the web plate (F_{WP}) due to internal shear stresses in the shell elements (σ_{xz}) is illustrated in Figs. 24 (b) and 25(b) for the B and NB wall, respectively. Fig. 24(c) shows the nodal reaction forces of the interface nodes (N_{CI}) of the concrete infill for the B model as a result of interaction with the HSS. Note that concrete infill is continuous for the NB model but, for illustration purposes the concrete part under the projection of the web plate was considered as infill concrete and the part confined by the half HSS was denoted as concrete core. Fig. 25(c) shows the shear force (F_{CI}) due to shear stresses (σ_{xz}) along the hypothetical plane section that defines the boundary of the concrete infill and the concrete core for the NB model. Figs. 24(d) and 25(d) illustrates the nodal reaction forces of the interface nodes of the HSS as a result of interaction with concrete infill (for only the B model) and concrete core (for both the B and NB models), and the axial force (F_{HSS}) due to axial stresses (σ_z) as a result of shear force from the steel web plate (F_{WP}), nodal reaction forces from the concrete infill (N_{CI}, for only B model) and concrete core (N_{CC}, for both the B and NB models). Figs. 24(e) and 25(e) illustrate the nodal reaction forces of the interface nodes of the concrete core as a result of the interaction with the HSS. For the B model, the axial force of the concrete core due to axial stresses is a result of the nodal reaction forces of the concrete core. For the NB model it is a result of the combination of nodal reaction forces and the shear forces from the infill concrete.

As shown in Fig. 24, vertical forces on the components of the boundary elements (HSS and concrete core) are the result of the vertical shear force of the web plate (F_{WP}), reaction forces of the interface nodes of the infill concrete (N_{CI}) and internal forces formed as a result of flexural deformation of the entire wall section (not shown in the figure). The contribution of vertical forces due to flexural deformation are negligible at locations far above the wall base where the curvature of the cross section is small (axial strains are small); it may become important at locations close to the wall base where the curvature of the cross-section is substantial (axial strains are high).

The axial force exerted on the concrete core is a result of interaction between the concrete core and HSS under lateral deformation of the wall owing to interface friction. The distribution of

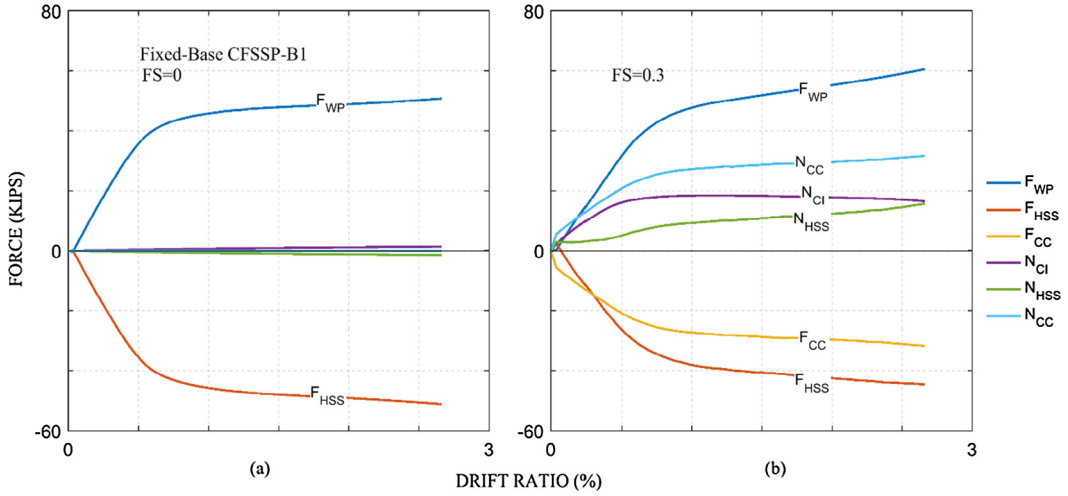

Fig. 26. Effect of interface friction in LS-DYNA model for CFSSP-B1: (a) FS = 0; (b) FS = 0.3.

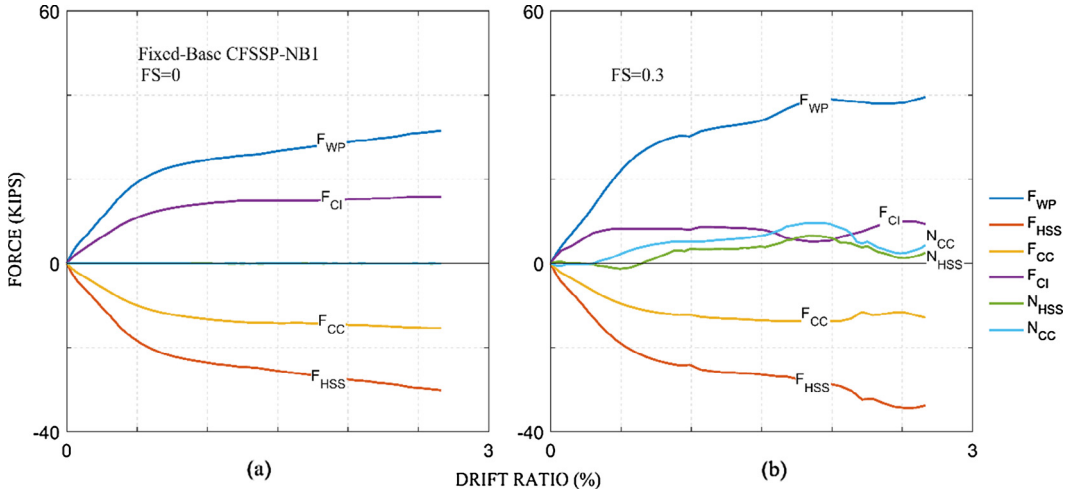

Fig. 27. Effect of interface friction in LS-DYNA model for CFSSP-NB1: (a) FS = 0; (b) FS = 0.3.

vertical forces (as a result of vertical shear forces from the steel web plate and reaction forces from concrete infill) between HSS and concrete core are interdependent and indeterminate.

Per Fig. 24, the equilibrium of forces in the vertical direction, assuming tension is positive, compression is negative, and positive force direction is upward, can be given as:

$$F_{WP} + N_{CI} = -(F_{HSS} + F_{CC}) \tag{4}$$

Note that for the NB model, N_{CI} in Eq. (4) should be replaced by F_{CI} per Fig. 25. Moreover, the vertical force equilibrium of the concrete force is; $F_{CC} = -N_{CC}$ for the B model, and; $F_{CC} = -N_{CC} - F_{CI}$ for the NB model.

A numerical study was conducted using LS-DYNA to investigate the interactions of the vertical forces for a partial section of the wall models illustrated in Figs. 24 and 25 for cases with interface friction (FS = 0) and without interface friction (FS = 0.3) between parts. Consider a fixed base LS-DYNA model for CFSSP B1 and NB1 specimens, modeled following the previously described element and material models. The models were subjected to lateral displacement at the top, and the response of the partial section (selected to be at the 100 in (2540 mm) wall elevation) of the wall top is investigated in terms of internal and external (nodal reaction forces) forces in the vertical direction.

Figs. 26 and 27 show the history of the vertical forces (F_{WP}, F_{HSS}, F_{CC}, N_{CI}, N_{HSS}, N_{CC}, see Figs. 24 and 25) of the partial section of the fixed-base LS-DYNA model for CFSSP-B1 and NB1 under positive lateral deformation, respectively. Fig. 26(a) shows the history of the results of the fixed-base B1 model that was assigned zero interface friction ($FS = 0$) for the contact model between steel and concrete parts. Due to lack of friction between interacting parts (concrete infill-HSS, HSS-concrete core) the nodal reaction forces (N_{HSS}, N_{CC}, N_{CI}) exhibited almost zero forces and thereby no vertical force is exerted on the concrete core; when that happens, the concrete core slips through the HSS. The equilibrium of vertical forces given in Eq. (4) is satisfied by having zero nodal reaction forces from the concrete infill ($N_{CI} = 0$), and zero axial force on the concrete core ($F_{CC} = 0$). Fig. 26(b) shows the history of the results of the model that includes interface friction between the interacting parts of the wall. Compared to the zero friction model, interface forces were created between the steel and concrete part which was added to nodal nodes (N_{CI}, N_{HSS}, N_{CC}) as shown in Fig. 26(b). Note that axial force on the concrete core is equal to nodal reaction forces of the concrete core ($F_{CC} = N_{CC}$). The shear force of the web plate is distributed between the members of the boundary elements (HSS and concrete core) and it satisfies the vertical force equilibrium given in Eq. (4).

Fig. 27(a) shows the history of the results of the fixed-base NB1 model that was assigned zero interface friction ($FS = 0$) for the contact model between steel and concrete parts, and shown that nodal reaction forces (N_{HSS}, N_{CC}) receive almost zero forces. These reaction forces increase under interface friction and satisfy the equilibrium given in Eq. (4).

8. Conclusion

The finite element study conducted in this paper has successfully replicated the cyclic inelastic behavior of the previously tested CFSSP-Walls and has provided insight into the behavior of CFSSP-Walls. Furthermore, the research reported here has provided insights in the following aspects of wall behavior that are of benefit for the design of similar walls. More specifically, it showed that:

- The smear-crack Winfrith concrete model is effective to capture the pinching behavior of the wall hysteresis;
- The distribution of wall base shear and moment forces between the embedded part of the wall and the foundation footing in the form of contact forces as well as shear forces created in the connector re-bars can be analytically quantified, and the results verify that the adopted design approach for the connector re-bars in the wall's footing is conservative as initially intended.
- The bottom row of tie bars in walls are subjected to large shear forces in the vertical direction due web plate buckling, which, for the NB1 wall model, reached the tie bar yield strength, but was less for the B1 wall model;
- Using the analysis results of the calibrated model, the cumulative plastic strain values at the onset of steel fracture is about ~1.40–1.45 in/in, which is a necessary value to determine low-cycle fatigue life of walls;
- The interaction of vertical axial stresses and horizontal stresses developed due to circular shape of the ends of the wall specimens is significant, as demonstrated by the plane stress distribution of the steel skin;
- Small discrepancies exist between the plastic neutral axis locations obtained analytically and numerically and that these are due to differences between the assumed and actual stress distributions in the compressed concrete;
- It is important to use an appropriate interface friction model to capture the complex relationship between the HSS and concrete core of the boundary elements, and that equilibrium equations developed here can be used to quantify the vertical forces created between the boundary elements and the effect of interface friction on the force flow within boundary elements.

Acknowledgements

This work was supported by American Institute of Steel Construction. However, any opinions, findings, conclusions, and recommendations presented in this paper are those of the writers and do not necessarily reflect the view of the sponsors.

References

[1] Alzeni Y, Bruneau M. Cyclic inelastic behavior of concrete filled sandwich panel walls subjected to in-plane flexure: Technical report MCEER-14-0009. Buffalo, NY: Multidisciplinary Center for Earthquake Engineering Research, State University of New York at Buffalo; 2014.
[2] Alzeni Y, Bruneau M. In-plane cyclic testing of concrete filled sandwich steel panel walls with and without boundary elements. J Struct Eng 2017 [in press].
[3] ABAQUS 6.13. [Computer software]. Dassault Systèmes Simulia, Providence, RI, USA.
[4] Goto Y, Kumar GP, Kawanishi N. Nonlinear finite-element analysis for hysteretic behavior of thin-walled circular steel columns with in-filled concrete. J Struct Eng 2010;136(11):1413–22.
[5] Imani R, Bruneau M. Post-earthquake fire resistance of ductile concrete-filled double-skin tube columns: Technical report MCEER-14-0008. Buffalo, NY: Multidisciplinary Center for Earthquake Engineering Research, State University of New York at Buffalo; 2014.
[6] LS-DYNA [Computer Software]. Livermore Software Technology Corporation, Livermore, CA.
[7] LSTC (Livermore Software Technology Corporation). LS-DYNA keyword users manual, vols. 1 and 2, version 971; 2015.
[8] ABAQUS. ABAQUS documentation. Providence, RI, USA: Dassault Systèmes Simulia; 2011.
[9] ACI Committee 318. Building code requirements for structural concrete and commentary. Farmington Hills, MI: American Concrete Institute; 2014 [ACI 318-14].
[10] Chen WF. Plasticity in reinforced concrete. New York: McGraw-Hill; 1982.
[11] Wittmann F, Rokugo K, Brühwiler E, Mihashi H, Simonin P. Fracture energy and strain softening of concrete as determined by means of compact tension specimens. Mater Struct 1988;21(1):21–32.
[12] Schwer L. The Winfrith concrete model: Beauty or beast? insights into the Winfrith concrete model. In: Proc., 8th European LS-DYNA users conference, 23–24; 2011.
[13] Epackachi S, Whittaker AS, Varma AH, Kurt EG. Finite element modeling of steel-plate concrete composite wall piers. Eng Struct 2015;100:369–84.
[14] Kurt EG, Varma AH, Booth P, Whittaker AS. In-plane behavior and design of rectangular SC wall piers without boundary elements. J Struct Eng 2016. 04016026.
[15] Hallquist JO. LS-DYNA theory manual. CA, USA: Livermore Software Technology Corporation; 2006. http://www.dynasupport.com/manuals.
[16] LS-DYNA. Keyword user's manual, vol. I. CA, USA: Livermore Software Technology Corporation; 2012 [Version 971 R6.0.0].
[17] Borrvall, T. Mortar contact algorithm for implicit stamping analyses in LS-DYNA <www.dynamore.de/de/download/papers/ls-dyna-forum-2012/documents/>; 2012.
[18] MacGregor JG, Wight JK, Teng S, Irawan P. Reinforced concrete: mechanics and design. Upper Saddle River, NJ: Prentice Hall; 1997.
[19] Prestressed Concrete Institute. PCI design handbook; precast and prestressed concrete. Chicago; 1971.
[20] ACI Committee 363. Report on high strength concrete. Farmington Hills, MI: American Concrete Institute; 2010.